Electrospun Copper Doped Titania Nanofibers for Dye-Sensitized Solar Cells Photoanode

By

Wajahat Qasim

Reg#00000319050

Session 2019-21

Supervisor

Prof. Dr. Zuhair S khan

U.S.-Pakistan Center for Advanced Studies in Energy (USPCAS-E)

National University of Sciences and Technology (NUST)

H-12, Islamabad 44000, Pakistan

March 2022

Electrospun Copper Doped Titania Nanofibers for Dye-Sensitized Solar Cells Photoanode

By

Wajahat Qasim

Reg#00000319050

Session 2019-21

Supervisor

Prof. Dr. Zuhair S Khan

A Thesis Submitted to the U.S.-Pakistan Center for Advanced Studies in Energy in partial fulfillment of the requirements for the degree of

MASTERS of SCIENCE

in

(Energy Systems Engineering)

U.S.-Pakistan Center for Advanced Studies in Energy (USPCAS-E)

National University of Sciences and Technology (NUST)

H-12, Islamabad 44000, Pakistan

March 2022

THESIS ACCEPTANCE CERTIFICATE

Certified that final copy of MS thesis written by Mr. Wajahat Qasim, (Registration No. 00000319050), of U.S-Pakistan Center for Advanced Studies in Energy, has been vetted by undersigned, found complete in all respects as per NUST Statues/Regulations, is within the similarity indices limit and is accepted as partial fulfillment for the award of MS degree. It is further certified that necessary amendments as pointed out by GEC members of the scholar have also been incorporated in the said thesis.

Signature: ______________________________

Name of Supervisor Dr. Zuhair S. Khan

Date: ________________________

Signature (HoD): ________________________

Date: ____________________________________

Signature (Dean/Principal): __________________

Date: ____________________________________

Certificate

This is to certify that work in this thesis has been carried out by **Mr. Wajahat Qasim** and completed under my supervision in Advanced Energy Materials and Systems Laboratory, U.S-Pakistan Center for Advanced Studies in Energy (USPCAS-E), National University of Sciences and Technology, H-12, Islamabad, Pakistan.

Supervisor:

____
Dr. Zuhair S. Khan
USPCAS-E
NUST, Islamabad

GEC member 1:

____
Dr. Naseem Iqbal
USPCAS-E
NUST, Islamabad

GEC member 2:

____
Dr. Nadia Shahzad
USPCAS-E
NUST, Islamabad

GEC member 3:

____
Dr. Sehar Shakir
USPCAS-E
NUST, Islamabad

HOD-ESE:

____
Dr. Rabia Liaquat
USPCAS-E
NUST, Islamabad

Dean/Principal:

____
Dr. Adeel Waqas
USPCAS-E
NUST, Islamabad

Acknowledgments

All praise to Allah Almighty who gave me the strength and knowledge to do the work presented in this thesis.

I would like to express my sincere gratitude to my research supervisor, Prof. Dr. Zuhair S. Khan for letting me be part of the research group at Advanced Energy Materials Lab, USPCAS-E, NUST, Islamabad. I feel privileged to have worked under his kind Supervision. It’s the blend of his patience, persistence, guidance, and motivation that made me accomplish my research aims in due time. He polished my research skills and I have learned a lot under his supervision and guidance.

I would like to sincerely thank my fellows and friends for their support. Especially, I pay gratitude to Lab Engineers Mr. Aamir Satti, Mr. Asghar Ali, Mr. Nisar Ahmad for their unmatchable support during the whole research work.

Abstract

Nanomaterials for photovoltaic have gained a lot of attention in the past few years in the arena of energy. Titania (TiO_2) is an important material having found its use in many technological applications. Due to its large surface-to-volume ratio, TiO_2 nanofibers (NFs) are drawing increased attention in 3rd generation of photovoltaic solar cells such as DSSC. The electro-optical response of TiO_2 can be tuned by metal doping and structural control at the nano level. In this research, NFs of copper (Cu) doped Titania (TiO_2) were fabricated by using electrospinning. To get Cu doped TiO_2 NFs the calcination and annealing were performed in the air at 500^{o}C for 2 hours. The Energy-Dispersive X-ray Spectroscopy (EDS) results confirmed the doping of copper inside the titania after calcination. Scanning electron microscopy (SEM) results show NFs of varying diameters mostly in the 80 nm to 200 nm regime. SEM of the post-annealed samples shows relatively rougher fibers of reduced size compared to the uncalcined samples which are due to the evaporation of PVP and solvents. The increase in roughness and reduction in the NFs diameter means an increase in the overall surface area and more efficient charge transport as Hall's effect results depicted that after doping of copper in nanofibers, the conductivity of the nanofibers improved by 2 times as compared to undoped nanofibers of titania. Moreover, Ultraviolet-Visible Spectroscopy (UV-Vis) showed that 1 % Cu doping decreased the bandgap and the absorption of the spectrum shifted more towards the visible region of the spectrum. The IV characteristic measurement was performed, and it gave the efficiency of the prepared solar cell equal to 0.0114 % with Open circuit voltage (V_{OC}) equal to 0.66 V and short circuit current (I_{SC}) equal to 0.03 mA. The increase in the V_{OC} is due to the wide bandgap of semiconductor and decreased diameter of nanofibers. The lower value of the I_{SC} is the result of Cu/electrolyte reaction and low electron injection of Nanofibrous Cu doped TiO_2 photoanode.

Keywords: Titania; Nanofibers; Cu-doping; Electrospinning, DSSC.

Table of Contents

List of Figures

List of Tables

List of journals/conference papers

1. “Electrospinning of Cu Doped TiO_2 Nanofibers and their Potential Application in Photoanode of Dye-Sensitized Solar Cells.” (International Conference Paper) W. Qasim, Z. Khan*, A. Satti, A. Ali , M. A. Shabbir , Z. Hussain.

   ISAM Conference Proceedings 2021, Journal of Key Engineering Materials, Scientific.net ISSN: 1662-9795. **(Under Review)**

List of Abbreviations/ Nomenclatures

DSSC	Dye Sensitized Solar Cell
CIGS	Copper indium gallium selenide solar cells
TCO	Transparent Conductive Oxide
NIR	Near-infrared
V_{OC}	Open Circuit Voltage
I_{SC}	Short Circuit Current
MPP	Maximum Power Point
P_{MP}	Power at MPP
V_{MP}	Voltage at MPP
I_{MP}	Current at MPP
FF	Fill Factor
NFs	Nanofibers
SEM	Scanning Electron Microscopy
EDX	Energy Dispersive X-Ray
EDXA	Energy Dispersive X-Ray Analysis
LNG	Liquefied Natural Gas
kW	kilo Watt
MW	Mega Watt
kV	kilo Volts
PV	Photovoltaic
I_D	Diode Current
I_{PH}	Photonic Current
I_S	Saturation Current of Diode
V_T	Thermal Voltage
PCE	Power Conversion Efficiency
HTMs	Hole Transport Materials

ZrO_2	Zirconium dioxide
Al_2O_3	Aluminum oxide
SiO_2	Silicon dioxide
TiO_2	Titanium dioxide
Cu	Copper
NPs	Nano Particles
TTIP	Titanium tetra chloride and titanium isopropoxide
UV-Vis	Ultraviolet–visible spectroscopy
EM	Electromagnetic
mm	Millimeter
cm	Centimeter
nm	Nanometer
eV	Electron Volt
FTIR	Fourier Transform Infrared Radiation
IR	Infrared Radiation
ASTM	American Society for Testing and Materials
J_{SC}	Short Current Density
FTO	Fluorine doped Tin Oxide
ITO	Indium doped Tin Oxide
C.E.	Counter Electrode

Chapter 1 Introduction

1.1 Energy Resources

In today's world, energy is the most fundamental requirement for human survival. Our creative exploitation and reinvention of energy are largely responsible development we have seen. Energy is used for industrialization, transportation, domestic and home use, and to meet the current era's normal lifestyle [1].

Despite the benefits that man's command of energy has provided, the rate at which energy has been exploited has put the environment in jeopardy. Finite resources are fast depleting, while carbon emissions continue to wreak havoc on the ecosystem on a global scale. Energy has been produced through the combustion of fossil fuels since its discovery. Greenhouse gas emissions from fossil fuels are extremely hazardous to all living beings on the earth. The increase in CO_2 levels is due to the combustion of fossil fuels in order to obtain energy in a suitable form. Increased CO_2 levels would result in air pollution, posing health risks to all living organisms as well as plants. Nitrogen oxide and Sulfur dioxide, which are created when fossil fuels are burned, can cause acid rain. Therefore, GHG emission is causing Global warming and environmental issues [2].

Global warming is not just raising the earth’s environment temperature, but it is also melting the ice, therefore, increasing the water level. Due to greenhouse gas effects, the ozone layer is also decreasing. There was a need for sustainable and environmentally friendly energy resources for so long. Numerous natural resources satisfy the energy needs of humans. Humans have been using coal, wind, water, and sun for thousands of years [3].

Renewable energy sources are one solution to the problem, and with more widespread adoption, they may one day power the entire world. Energy resources include all types of fuels employed in the world today for electrical energy generation, heating, and other energy conversion operations. Energy resources can be classified into two: Non-Renewable and Renewable [4].

Non-renewable resources are abundant but finite, and they are not renewable. These energy resources come from the decomposition of dead plants and animals that have accumulated during the planet's lengthy history. Natural gas, oil, and coal are the most common of these resources. Renewable energy resources are naturally replenished over time. Traditional renewable resources include solar, wind, geothermal, tidal, wave, biomass, and hydropower [5].

1.1.1 Non-Renewable Energy Sources

Nonrenewable resources are finite and cannot be exploited forever. Coal, natural gas, oil, and nuclear energy are the four principal types of nonrenewable resources. Fossil fuels were produced inside the Earth over a time of millions of years from dead plants and animals, and thus the term "fossil" fuels are used. Radioactive materials, primarily uranium, are taken from mined ore and converted into fuel to provide nuclear energy [6].

Nonrenewable energy sources:

1. Coal
2. Natural gas
3. Petroleum
4. Nuclear energy

1.1.1.1 Coal

A combustible black sedimentary rock with a high carbon and hydrocarbon content. Because coal takes millions of years to create, therefore it is classified as a nonrenewable energy source. Coal is made up of the energy stored by plants that thrived in marshy forests hundreds of millions of years ago. Over millions of years, layers of earth and rock layered over plants. As a result of the heat and pressure, the plants were transformed into coal. 1 short ton of coal is equal to 18,856,000 Btu [6,8].

1.1.1.2 Natural Gas

Natural gas was created deep beneath the surface of the earth. Natural gas is made up of a variety of chemicals. Methane, a molecule having four hydrogen atoms and one carbon atom (CH_4), is the most abundant component of natural gas. Natural gas also comprises non-hydrocarbon gases including water vapors and carbon dioxide, as well as natural gas liquids (NGLs), which are also hydrocarbon gas liquids. Natural gas is used as a fuel and to manufacture chemicals and materials [6,8].

1.1.1.3 Oil and Petroleum

Petroleum and oil fossils are hydrocarbons created from the leftovers of animals and plants that lived in a marine environment millions of years ago before the dinosaurs existed. The remnants of these creatures and plants were covered by rock, salt, and sand layers over millions of years [7,8]. The residues were transformed into crude petroleum or oil as a result of the pressure and heat exerted by these layers. Petroleum is short for "rock oil" or "earth oil.”. The crude oil could be found in underground reservoirs, small gaps inside sedimentary rocks, and near the earth's surface in gaseous or liquid form. Petroleum products are fuels manufactured from crude oil and natural gas hydrocarbons. Natural gas, biomass, and coal all can be used to make petroleum products [6,8].

1.1.1.4 Nuclear energy is energy in the core of an Atom

Atoms make up solids, liquids, and gases. Protons, electrons, and neutrons are the three particles that make up an atom. The nucleus of an atom is made up of neutrons and protons and is surrounded by electrons. The bonds that hold the nucleus together contain a tremendous amount of energy. When those bonds are broken, nuclear energy can be released. Nuclear fission can break the bonds, and the resulting energy can be utilized to generate electricity [6,8].

1.1.2 Renewable Sources

Renewable energy is derived from natural resources and is replenished regularly. Renewable energy sources include water, wind, sun, plants, and Earth's heat, all of which are perpetually renewed by nature. Renewable energy technologies convert these fuels into useable energy, such as electricity, mechanical power, chemicals, or heat. Renewable energy can be used in a variety of ways. In our daily lives, most of us are already using renewable energy.

Renewable energy comes in many different forms [9].

1. Solar Energy
2. Wind Energy
3. Hydro Energy
4. Bio Energy
5. Geothermal Energy
6. Ocean Energy

1.1.2.1 Solar Energy

Technologies used for solar energy harness the sun's limitless power and utilize it to generate electricity, light, and heat. There are different ways solar energy can be used [10,11].

1.1.2.2 Solar Water Heating (SWH)

The energy coming from the sun can be utilized to heat water in your swimming pool or any water at home. A solar collector and a water storage tank are the most common components of SWH systems. Mostly collectors are installed on a roof facing south, which uses either the fluid for heat transfer such as nontoxic antifreeze to heat space or heat water, in SWH. After that, the hot water is kept in the tank like the tank that can be found in an electric water heater or standard gas heaters. Solar collectors for water heating can be divided into three categories: evacuated tube type collector, flat plate type collector, and concentrating type collector [10,11].

Passive Solar Heating/Lighting

For generations, the sun has always been used to heat homes and places. As fans, no pumps, or other mechanical devices are utilized, the modern type of this sun-welcoming design is known as passive solar. Large windows that are facing south, feed homes with light, while brick floors or dark tile can store the heat coming from the sun and can be used to heat the home at night [11]. Window overhangs block direct sunlight in the hot season, when the sun is at its peak in the sky, maintaining the house at a lower temperature. In summer, tile and stone flooring is also used to cool [10,11].

Solar Electricity

Photovoltaic (PV) technology, sometimes known as solar electricity, turns sunlight directly into electricity. Since the beginning of space programs, solar electricity has been a primary source that is used to power spacecraft. For the previous three decades, it is employed as an electrical power device in addition to agricultural and rural purposes. Because of breakthroughs and global developments in the field of electricity, it has formed a large market for powering grid-connected homes and buildings over the previous decade. Although there are many different types of solar electric systems on the market today, mainly they have three components: Modules that are used to convert sunlight into electric current, inverters that convert the generated direct current into alternating current, and sometimes storage systems such as batteries that could store surplus power, generated by solar modules. This generated electricity is used by most household appliances [10,11].

1.1.2.3 Wind Energy

For hundreds of years, windmills have been used to harness the energy of the wind. These days wind turbines can be employed instead of windmills and are far more improved and efficient technology. Although wind turbines appear to be noncomplex, it involves a series of steps to generate electricity. The wind first turbine blades rotate and are attached to the shaft. This moves the generator, which generates electricity. The energy is converted into electricity using modern mechanical drive systems and power generators. Wind turbines that inject power into the grid range in size from 50 kW - 0.5 MW. A large number of turbines are scattered throughout the land for large-scale utility operations [10,11].

1.1.2.4 Hydro Energy

Hydropower is the most established renewable energy source. Hydropower facilities generate electricity by converting the energy contained in moving water. A common type of hydropower involves retaining a big reservoir of water by building a dam on a river. Water through the turbine is released to generate electricity. Hydropower stations are mostly environment friendly, but they can impact wildlife habitats and the quality of water. As a result, hydropower plants are constructed and with minimum impact on rivers [10,11].

There are three different types of hydropower facilities: diversion type in which diversion of a river is used to produce energy. Impoundment type which uses a dam to store river water then the water released from the reservoir to generate the energy. Pumped storage type in which pumping water from a lower to an upper reservoir is done to preserves energy. When there is a significant electrical power demand, the water is discharged into the penstock, where it drives the turbine and produces electricity. Some hydropower plants use dams, and some do not [10,11].

For storage of energy the water pumping from lower to an upper tank can be done. When there is a significant energy requirement, the water is then discharged into the reservoir. situated at lower height or pool, where it moves a turbine, which in turn produces electricity [11].

1.1.2.5 Bio Energy

Bioenergy is obtained from biomass for example grass, plants, vegetables, etc. is known as bioenergy. A simple example of bioenergy is the burning of wood. However, all of the biomass resources are not obtained from plants. Many industries, like industries that involve the processing of agricultural products and construction, can produce a substantial amount of residual or unutilized biomass that can be used to produce bioenergy. Biomass may also be converted directly into biofuels that are biomass-based liquid fuels. To fuel stationary power generation and cars, biofuels are preferred as they can be transported conveniently, and their energy density is high. Ethanol is the most common type of biofuel [10,11].

1.1.2.6 Geothermal Energy

The core of the Earth is located 6437.4 kilometers beneath the surface and can reach temperatures up to 4982 degrees Celsius. This generated temperature spreads outward from the core, therefore warming the surroundings and perhaps generating subterranean steam reservoirs and hot water. We can use these reservoirs for different purposes, including electricity generation, and building heating. By Installing Geothermal Heat Pumps (GHPs) we can even utilize the ground’s consistent temperature for cooling and heating houses and other buildings [10,11].

1.1.2.7 Ocean Energy

There are two sorts of energy that the ocean can produce using ocean energy. The tides and waves energy provide mechanical energy. The thermal energy stored in the ocean which derived from the heat of the sun. In Ocean thermal energy is used to run a turbine, which is attached to a generator. Therefore, conversion to electrical power is done. Mechanical devices are commonly used for the conversion of tidal and wave energy into electricity. A dam can be used to convert tidal energy into electrical power. This is done by pushing water through turbines, which in turn runs a generator. Wave energy can be used to move mechanical parts attached to a generator to generate electricity. In other cases, working fluids like air and water can be used to run the generator or turbine [10,11].

1.2 Energy Mix in Pakistan

In the past, Pakistan has overcome its energy crisis, which directly or indirectly affected the economy, by increasing its generation and transmission capacity. Currently, the Energy Sector has a demand-supply imbalance that must be filled by improving the energy mix to reduce costs. Pakistan's dependence on thermal energy, which includes imported coal, domestic coal, LNG, and natural gas, has decreased in recent years [12].

1.2.1 Non-Renewable Energy in Pakistan

1.2.1.1 Oil Sector in Pakistan

Pakistan consumes 19.68 million tons of petroleum products per year, with local refineries supplying 11.59 million tons and imports accounting for the remaining 8.09 million tons per year. Consumption of petrol in Pakistan is 7.6 million tons per year, with 30% coming from local refineries and the balance coming from outside to meet national demand. Diesel consumption is also around 7.3 million tons per year. Local production can meet 65 percent of total demand, with the remainder requiring importation [12,16].

1.2.1.2 Coal Production/Consumption in Pakistan

The country has a vast energy resource in the form of coal, and further development in various places is underway, out of which a fraction is being used. Local coal consumption should be increased in the next years to achieve a larger contribution. The Thar coal field is home to a slew of coal mining and power generation plants. Imported coal power stations could be used, combined with Thar Coal. The use of Thar coal is limited as spontaneous combustion is a probable hazard for long-term storage and distant transportation. power plants utilizing imported coal have begun operations, including one in Sahiwal, two in Port Qasim, and one in Thar [12,16].

1.2.1.3 Gas Sector in Pakistan

Natural gas is a nonrenewable energy source that is clean, safe, efficient, and better for the environment [18]. Natural gas account for 38% of Pakistan's primary energy mix. Pakistan produces roughly four billion cubic feet per day (Bcfd) locally, compared to a demand of over six billion cubic feet per day (Bcfd). To fill this gap, the government of Pakistan has to import importin Liquified Natural Gas (LNG). Pakistan has a vast gas network of gas pipelines (139,827 km distribution, 37,058 km service, and 12,971 km transmission pipelines) to meet the needs of the country [12,16].

1.2.1.4 Nuclear Sector in Pakistan

The country's only department that handles the power generations using nuclear-powered power plants is Pakistan Atomic Energy Commission (PAEC). There is a total of five nuclear power plants in Pakistan, one of which is the Karachi Nuclear Power Plant installed in Karachi and the other four are named the Chashma Nuclear Power Plants with four units in Chashma which is a district of Mainwali. These five nuclear power reactors can generate 1430 MW and they have produced around 7,143 million units from July 2019 to March 2020 (11 months period). PAEC is also working on K-2 and K-3 projects to meet the goal of 2200 MW set for 2030 [12,16].

1.2.2 Renewable Energy in Pakistan

1.2.2.1 Production of Energy from Solar

Pakistan has a lot of solar power potential. The potential for Solar Energy is predicted to be more than 100,000 megawatts (MW). The average irradiation across the country is between 4.5 (kWh/m^2)/day and 7.0 (kWh/m^2)/day. The Alternative Energy Development Board (AEDB) was formed by the ministry of energy Pakistan. It is working on 22 solar Photovoltaic (PV) power projects with an approximate total capacity of 890.80 MW.

Figure 1-1: Quaid-e-Azam Solar Park with a capacity of 1,000 MW [17].

1.2.2.2 Production of Energy from Wind

The capacity of the power from wind energy is considerable along the 1,000 km of coastline in Sindh and Baluchistan's southern areas, where wind speeds from 5 m/s to 7 m/s. Wind energy has a potential capacity of 122.6 GW/annum, which is more than quadruple the country's existing power-producing capacity. A finished wind farm installed in Gharo in Sindh (Pakistan), is among a chain of projects being built throughout the country to help in the energy shortage. In 2019, Pakistan had more than around 1000 MW of operating wind farms [12,16].

1.2.2.3 Production of Energy from Hydro

The country has a hydropower potential of 60,000 MW, however, only 7,320 MW of the projects has been developed. Tarbela Dam is the biggest dam which has a capacity of 4888 MW. Pakistan hydropower also includes other big and small dams. The majority of the plants are located in the Chitral and Northern Areas that are community-based. Small hydropower is another interesting alternative for generating electricity for off-grid. The minor hydropower sector was mostly controlled by provincial governments in 2014. The country has 128 MW of operational capacity, 877 MW of capacity under construction, and roughly 1500 MW of capacity available for future expansion. A 350 MW of the potential of micro-hydro projects in Punjab is present, and in northern Pakistan, 300 MW [12,16].

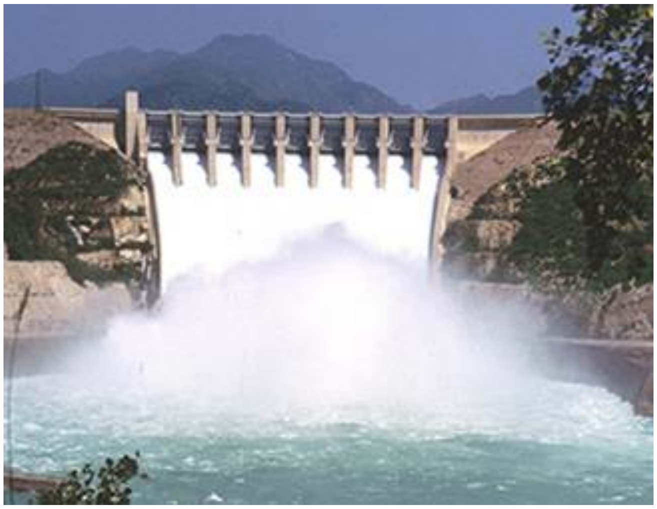

Figure 1-2: Tarbela Dam, Khyber Pakhtunkhwa, Pakistan [18].

1.2.2.4 **Production of Energy from Biomass**

In Pakistan 21.2 million hectares are cultivated. Pakistan is the largest contiguous irrigation system in the world. Forests span over 4.21 million hectares, accounting for 5% of the country's total land area. According to Food and agriculture organization of United Nations data, these numbers have been steadily declining since the 1990s, and in 2015, it was only 1.9 percent [12,16].

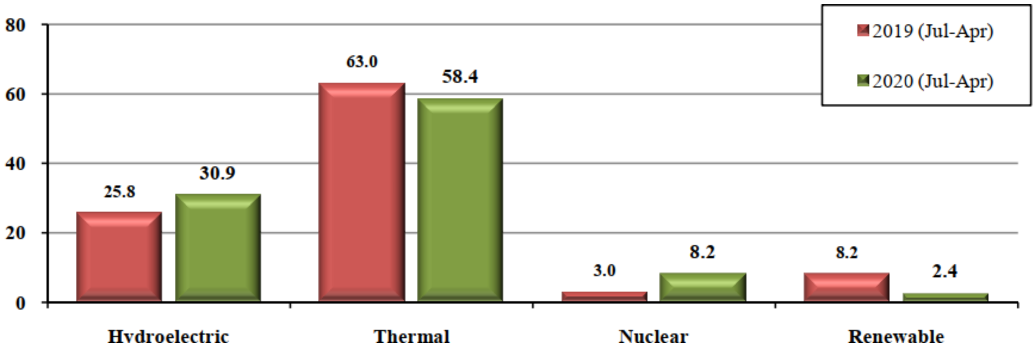

Figure 1-3: Share of different Energy resources in Electricity Generation (%) of Pakistan [12].

1.3 Photovoltaics Technology

The "photovoltaic" is derived from the Greek word photos which means light and voltaic from the scientist named Alessandro Volta, which could also mean voltage. Therefore, the term photovoltaic could mean the light source. In order to extract energy, with solar radiation as the primary source of energy photovoltaics cell or solar cell is required [19].

1.3.1 Solar Radiations

The Sun is a massive fusion reactor, in which many four hydrogen atoms fuse together to form one helium atom within. Atomic fusion produces temperatures of roughly 15 million ° C. Radiations transfer this energy from the sun into space. The Sun constantly emits 38451026 W throughout space in every direction, out of which a small fraction is received by Earth receives. The fraction of solar energy is 1367 W/m^2 which is known as the Solar constant [20].

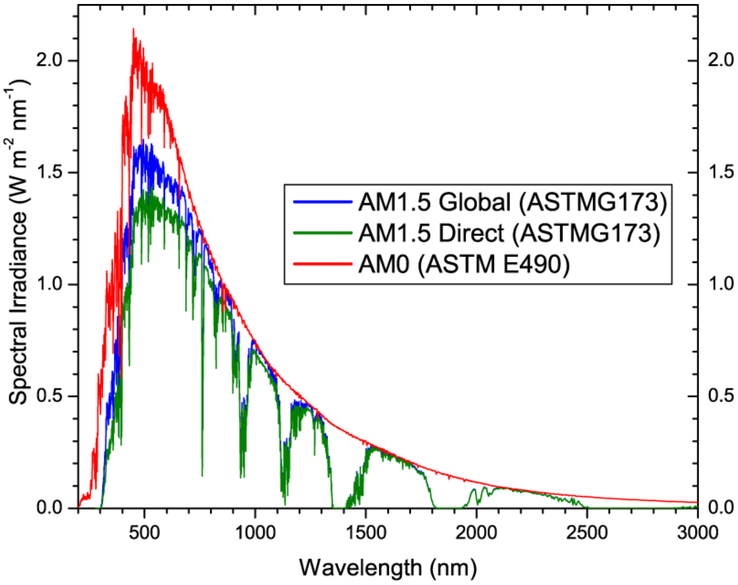

Figure 1-4: A Solar Spectrum for terrestrial and space [21].

Radiations are emitted by every heated body into the environment. Planck's Law of Radiation states that the spectrum of radiation is determined by the surface’s temperature. The surface temperature of the Sun is 5778 K, resulting in the ideal spectrum called Black Body Spectrum. Outside the Earth's atmosphere (AM0), the real spectrum roughly trails this line. This light hasn’t traveled through the earth's atmosphere, as indicated by AM0 known as Air Mass “0”. It is indicated by the red line in figure 1.4 [21].

1.3.2 Working (Conversion of light to current)

Typically, solar cells consist of semiconductors. Structurally it consists of an anode and a cathode. An example of a silicon-based solar cell is a PN junction (photodiode). Where P-type is doped with a tri-valent impurity for example boron and N-type semiconductor is doped with a pentavalent impurity (phosphorus). N-type has excessive electrons as charge carriers and P-type has excessive holes as charge carriers. Other parts may include antireflection coating and front and back contacts [22].

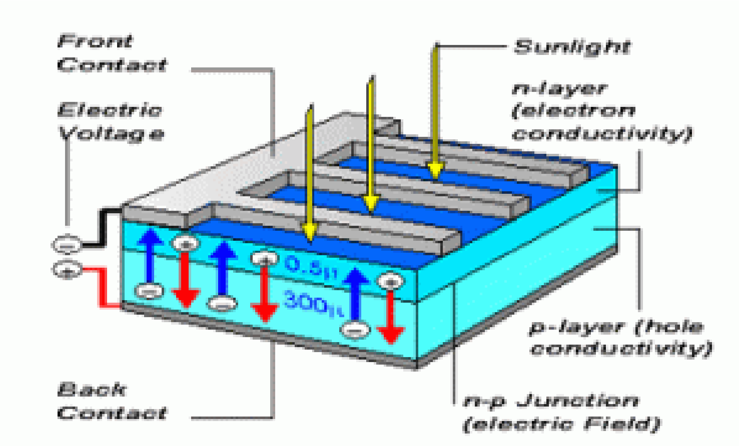

Figure 1-5: A typical solar cell [19].

The structure of the typical solar cell is shown the figure 1.5. Whenever light shines upon the solar cell the solar energy is converted into electrical energy. The energy conversion of solar to electrical in photoelectric devices involves the following steps [19].

a) The light is absorbed by the semiconductor material.
b) Excitation of the atoms from the ground state to an excited state.
c) Conversion of excited atoms to positive and negative charges.
d) The generated charge carries, move towards the electrodes.
e) The carries are collected by an external circuit.

Recombination of the carriers after flowing through an external circuit. Therefore, completing the cycle. For Photodiode Shockley equation can be used to express its electrical behavior. This electrical behavior can be represented by an equivalent electrical circuit as shown in figure 1.6.

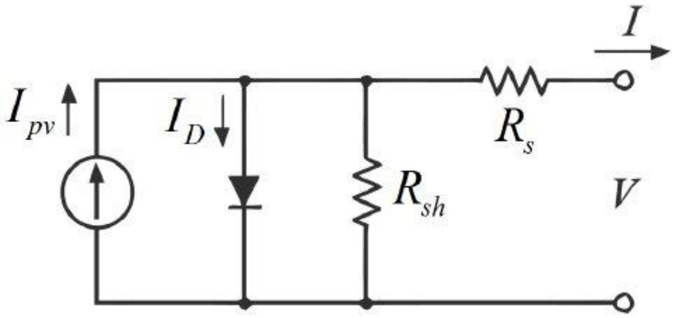

Figure 1-6: An Equivalent circuit model of PV solar cell [26]

$$\boldsymbol{I = I_D - I_{Ph} = I_S.\left(e^{\frac{V}{V_T}} - 1\right) - I_{Ph}} \qquad \textbf{(1.1)}$$

Where

I_D = Diode Current.

I_{PV} or I_{Ph}= The photonic current or photocurrent.

I_S = The saturation current of the diode.

V =The voltage applied to the device.

V_T = Thermal Voltage.

All the parameters of the solar cells could be defined by the characteristic curve. The principle of the solar cell corresponds to the characteristic curve as shown in figure 1.7. Looking at the curve following parameters could be defined

1.3.2.1 Parameters effecting on Solar cell

a) Short Circuit Current I_{SC}

When the circuit of the solar cell is shorted I_{SC} is delivered with a voltage equal to zero. On the curve, it is the point when Voltage is zero [19]. This gives

$$\mathbf{I_{SC}=I_{Ph}} \tag{1.2}$$

b) Open Circuit Voltage (V_{OC})

When the current is zero V_{OC} is obtained. On the curve, it's the point when the current is zero [19]. When we substitute the parameters, we get

$$\boldsymbol{V_{OC} = V_T . ln\left(\frac{I_{SC}}{I_S} + 1\right)} \tag{1.3}$$

c) Maximum Power Point (MPP)

MPP is an operating point at which maximum power is obtained. Corresponding voltage and current points are called V_{MPP} and I_{MPP} respectively.

d) Fill Factor (FF)

Fill Factor is the ratio of MPP and product of V_{OC} and I_{SC}. On the curve, it's the area under MPP compared to the area of V_{OC} and I_{SC}

$$\boldsymbol{FF = \frac{P_{MPP}}{V_{OC} . I_{SC}}} \tag{1.4}$$

e) Efficiency (η %)

The efficiency of the solar cell is defined as the ratio of obtained electrical power to incident optical power [19]. Mathematically

$$\boldsymbol{\eta = \frac{P_{MPP}}{P_{OPT}}} \tag{1.5}$$

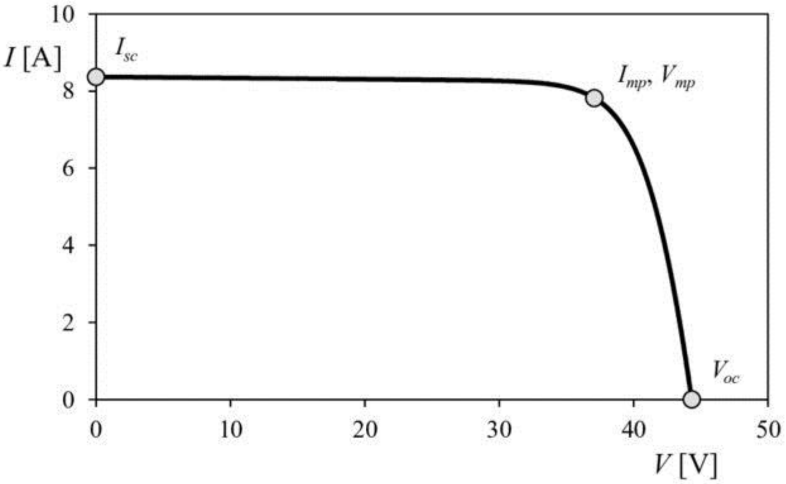

Figure 1-7: IV Curve of a Solar Cell with other parameters [26].

1.2.4. Generations of Photovoltaics

Depending upon the technology and material used, the solar cells are divided into three generations.

1.2.4.1 First Generations (1^{st} Gen) of Photovoltaic

Solar cells of the first generation are typically silicon-based. Solar cells made of crystalline silicon typically have a (15 to 20) % efficiency. The thickness is of first-generation solar is 100s of μm.

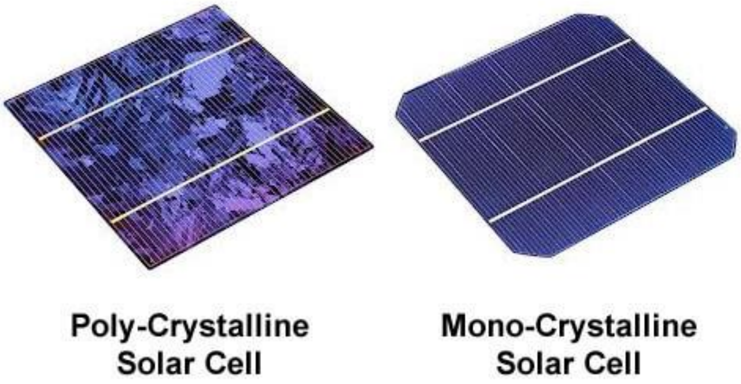

Figure 1-8: Mono-Crystalline and Poly-Crystalline Solar cells [24].

These solar cells are extremely stable, however, the technology utilized to make first-generation solar cells are highly energy-intensive, hence necessitating the development of less energy-intensive solar cell production techniques. Secondly, the cost of first-generation solar cells is extremely high due to the high cost of highly pure silicon. These factors prompted the development of a new generation of solar cell types. The production share of first-generation solar cells is more due to improved industrial-scale manufacturing [21].

1.2.4.2. Second Generations (2nd Gen) of Photovoltaic

Thin-film silicon and nanocrystalline, amorphous silicon, semiconduction-based thin-film solar cells are the second generation of solar cells. Examples of second generations solar cells are CdTe and CIGS. Second-generation photovoltaics have an efficiency of roughly 10%. When compared to first-generation solar cells, these solar cells are much easier to make and have lesser cost/unit [21].

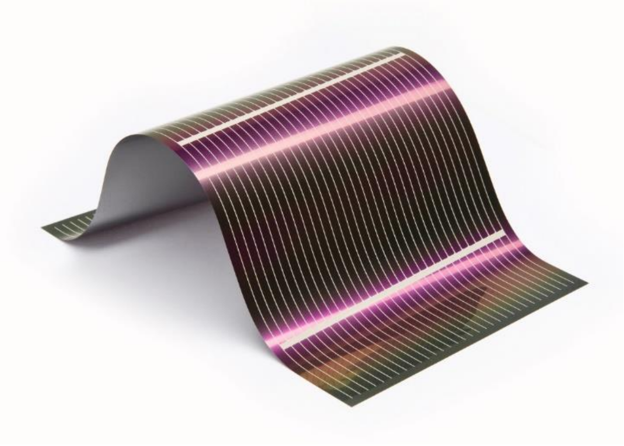

Figure 1-9: A Second-generation thin-film solar cell [22].

1.2.4.3. Third Generations (3rd Gen) of Photovoltaic

Solar cells of the third generation are quite essential due quantity of research being done in this field. These are thin-film solar cells. Examples of solar cells are CZTS, DSSCs, Perovskite solar cells. Polymer solar cells and organic Photochemical-based solar cells are further examples. The efficiency of these sorts of solar cells can reach is around 15%. The materials used to make them are plentiful and they are simple to make. Multi-junction solar cells, which are the most efficient solar cells, also lie in the third-generation solar cells. The energy band gap in third-generation solar cells may be adjusted by modifying the materials and varying the technology, allowing broad wavelengths of light to be utilized successfully [21].

Figure 1-10: Dye-sensitized solar cells integrated SwissTech Convention Center made by Solaronix [27].

1.4 Dye-Sensitized Solar Cells

Due to the ease of its manufacturing technique under ambient circumstances, dye-sensitized solar cells (DSSCs), which are classified as third-generation photovoltaics, have been presented as a low-cost substitute to traditional silicon solar cells. due to simplicity in fabrication. Michael Gratzel and Brian O'Regan designed modern DSSCs, also known as Gratzel cells, in 1988. In the late 1960s, it was found that when illuminated with light organic dyes could produce energy at oxide electrodes, while researching the electrodes for electrochemical cells. After that, different attempts were done to investigate the underlying mechanism in photosynthesis, which resulted in numerous tests for generating electricity using the DSSC since 1972 [25].

A DSSC is generally a thin layer of an anode made of a suitable metal oxide. This layer of the anode of coated onto glass with a conductive oxide coating. On this layer of metal oxide, a dye is sensitized. These parts make up an anode. While cathode consists of

Transparent Conductive Oxide (TCO) with Platinum film coating. An electrolyte solution is placed between anode and cathode usually made of iodide/triiodide [26,27].

1.5 Working Principle of DSSCs

1.5.1 Working Principle of DSSCs

Dye-sensitized solar cells do not follow the typical silicon-based solar cells principle; instead, distinct components perform the light absorption and charge transfer roles. The semiconductor's principal role is to promote charge transmission, while the dye is employed to absorb photons. The advantages of DSSCs over conventional p-n junction solar cells are numerous. Here are some of the benefits of DSSCs in comparison with silicon-based solar cells [1].

Low-cost production, as well as material flexibility, including substrates, and the ability to operate over a wide temperature range, are all advantages of DSSCs [1].

1.5.2 Working of components inside the DSSCs

The dye's electrons are stimulated by incident sunlight. The energized electron travels to the electron collecting glass substrate after being injected into the metal oxide's conduction band. The electron travels from the anode to the counter electrode via the connected circuit, to obtain valuable power. The oxidized dye is regenerated by the electrolyte's reducing agent. The oxidized species of the electrolyte is reduced to its original condition once the electron has traveled through the load and been collected at the counter electrode. The circuit is now complete, and the cycle flow of electrons from the anode to the cathode continues [2].

In DSSCs, charge separation occurs by kinetic competition. Whereas, in p-n junction solar cells, charge separation takes place by the formation of the electric field in the junction. Photon to energy conversion in DSSCs takes place in the following steps [15].

There are four different processes (steps) involved in the working of DSSCs [17].

1) Light Absorption
2) Electron Injection

3) The charge carries (Current) Transportation
4) Charge carrier (Current) Collection

1.5.2.1 Light Absorption

Light is absorbed by the dye and this absorption of photons excites the dye molecules from HOMO (Highest occupied molecular orbital) to LUMO (Lowest unoccupied molecular orbital) states. It takes nearly 60 ns to excite an electron for HOMO to LUMO [17].

$$\mathbf{S^{+}/S\ (ground\ state) \rightarrow (S^{+}/S^{*})(excited\ state)} \qquad (1.6)$$

1.5.2.2 Electron Injection

The excited electron is transferred from dyes LUMO to the conduction band of the semiconductor. For efficient electron injection, the energy level of the semiconductor conduction band must be about 0.2 V - 0.3 V lower than that of dye. The back reaction of the electron from the conduction band to the oxidized dye molecule is much slower and lies in the microsecond to millisecond range. This difference causes efficient charge separation in the cell. It takes nearly 50 femtoseconds −1.7 picoseconds to transfer an electron from LUMO to the conduction band [17].

$$\mathbf{S^{+}/S\ (ground\ state) \rightarrow (S^{+}/S^{*})\ (excited\ state) + e^{-}\ (TiO_2)} \qquad (1.7)$$

1.5.2.3 Charge carrier (Current) Transpiration

Electron diffuses through the photoanode, reaches TCO, and travels to the outer circuit to generate electric power (flow of electrons). In TiO_2 based nano-porous photoanode, the layer contains anatase nanoparticles. The presence of oxygen vacancies in the TiO_2 lattice makes it slightly n doped. The plane (101) is thermodynamically stable and is predominant in TiO_2 anatase nanoparticles. The electron transport within the TiO_2 layer occurs through diffusion since the nano particles are very small to form an electric field. The electron transfer can be explained by the trapping/detrapping model. Electron waits in the trap state for time t before hopping to the next trap site. The trap state waiting time depends on the depth of the trap state. Since the transport of electrons takes place by diffusion, the diffusion length of electrons must be greater or at least equal to the thickness of the photoanode. The optimized thickness of the TiO_2 layer in photoanode varies from 5 μm to 15 μm [17].

1.5.2.4 Charge carrier (Current) Collection

After the flow of electrons through the outer circuit, it is collected at the counter electrode (C.E). Regeneration of dye and electrolyte involves recombination of the charge carriers. Regeneration of dye takes some nanoseconds and for electrolytes, it takes 10 microseconds [16].

$$\mathbf{(S+/S^*)\ (excited\ state) + e- \rightarrow S+/S\ (ground\ state)} \qquad (1.8)$$

$$\mathbf{I^{-3}+2e^{-}\rightarrow 3I^{-}} \qquad (1.9)$$

Electron after reaching counter electrode is transferred to the electrolyte which consists of a redox couple. This electron regenerates the oxidized dye molecule in the nanosecond timescale range. A loss of about 600 mV occurs which is the main reason which limits the V_{OC} of the cell. The loss occurs due to a mismatch of energy between the redox couple and the dye [16].

The complete steps of a photon to current generation mechanism in DSSCs is shown by the equations 1.8 to 1.12 where S is dye molecule, S* excited dye molecule, S^+ oxidized dye molecule, and e^- represents an electron.

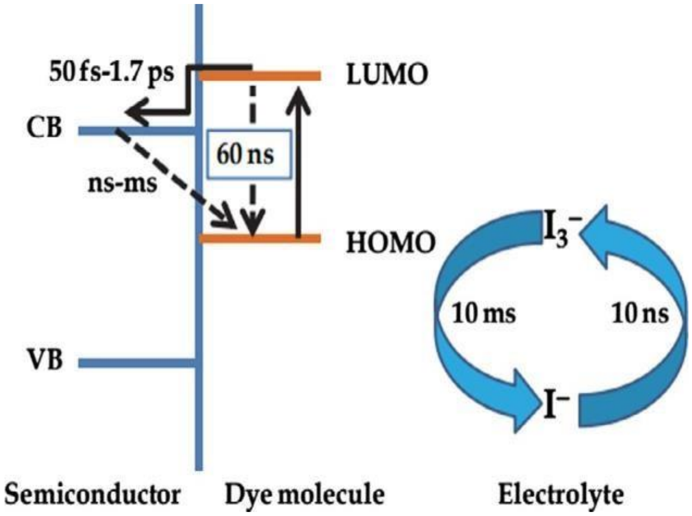

Figure 1-11: Kinetics of charge transport [39].

1.6 Components of DSSCs

Conventionally DSSC is constructed of the substrate (electrode), a metal oxide semiconductor, Electrolyte, Dye sensitizer, and conductive counter electrode as shown in figure 2.2 [28].

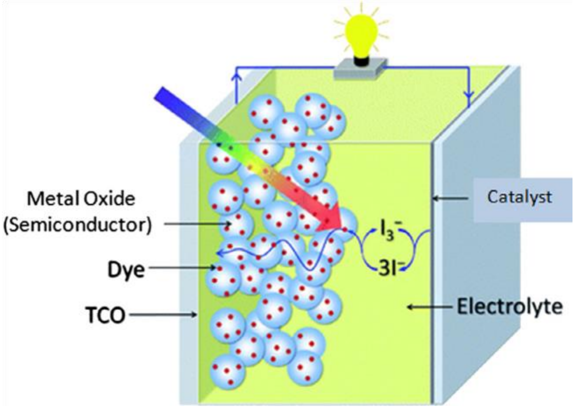

Figure 1-12: Components of DSSCs [40].

1.6.1 Substrates for DSSCs

It is naturally transparent, and it allows the solar radiation to pass through. Clear glass substrates with great optical transparency in the Visible and NIR regions are the most often used substrates in DSSCs. The solar radiations are absorbed by the photoactive material (Semiconductor) deposited on this substrate. Other functions of the substrate include a collection of current therefore it should be a good conductor. On one side of the glass, the substrate is a thin sheet of transparent conducting oxide that works as a low-resistance conductive film. On glass substrates, indium-doped tin oxide (ITO), or fluorine-doped tin oxide (FTO) are most often deposited as a transparent conductive oxide. The device performance depends on the transmittance of light and the conductance of the substrate [29].

1.6.2 Types of Electrolytes for DSSCs

The electrolyte is a DSSC component that is responsible for electron transport as well as the regeneration of oxidized dye. The main function of electrolytes is the regeneration of dye. The electrolyte is composed of a redox couple, and it is placed between the electrodes

(Cathode and Anode). Types of electrolytes being used for DSSCs are Liquid (most used), quasi-solid state, and solid-state electrolyte [37].

1.6.2.1 Liquid Electrolytes for DSSCs

Liquid electrolytes generally contain a redox pair, suitable organic solvents (for solutes dissolution), and additives (for solution stability/Viscosity). Each component of a liquid electrolyte, such as the redox couple and the solvent or additive, affects photovoltaic performance. An organic solvent creates a favorable environment for redox ion dissolution and diffusion. The dielectric constant of the solvent, its viscosity, and its donor number are the most essential features of organic solvents. Because ion conductivity is dependent on solvent viscosity, therefore a low viscosity solvent is preferable. The more viscous the solvent, the poorer the ion conductivity and the worse the cell performance. The (I^-/I^{-3}) redox pair is the most used due to its low cost and simplicity of manufacture. As a result, it is commonly employed as a standard electrolyte in DSSC photoanode and dye performance testing [36].

1.6.2.2 Quasi Solid-state Electrolyte for DSSCs

The gel state, also known as the quasi-solid state, is neither liquid nor solid. A polymer host is filled with liquid electrolytes in quasi-solid-state electrolytes. Despite their high viscosity, these electrolytes have the diffusive properties of a liquid and the cohesive properties of a solid, resulting in strong interfacial contact and high ionic conductivity. They also exhibit a high level of stability [38].

1.6.2.3 S**olid-state Electrolyte for DSSCs**

Solid-state electrolyte-based DSSCs have an I^-/I^{-3} redox pair and operate similarly to liquid electrolyte-based DSSCs. Hole Transport Materials is an example of a solid-state electrolyte (HTMs). The sole difference in the operation of HTM-based DSSCs is that the oxidized dye molecule is deoxidized by an electron given by the hole conductor. As electrolyte materials in DSSCs, copper based inorganic HTMs (CuBr, Cul, and CuSCN) are employed. They have strong hole-carrying capabilities; however, they are inefficient and unstable. Due to increased recombinations and lower intrinsic conductivities of HTMs, HTM-based DSSCs have poorer efficiency than liquid electrolyte DSSCs [39,40].

Therefore, for the electrolyte to be good.

1) Regeneration of the dye molecule to its ground state should be fast.
2) It Should have higher conductivity for fast diffusion.
3) Higher stability (Chemical, Thermal, and Optical)
4) It should not absorb the light in the visible range.
5) Good interfacial contact between photoanode and counter electrode.

1.6.3 Photoanode materials for DSSCs

Photoanode is constructed of a mesoporous structure and metal oxide semiconductor. It provides two functions which are dye adsorption and charge carrier collection and transport. Power conversion efficiency (PCE) greatly depends upon the porosity, conduction band, surface area, and crystallinity of the photoanode. Photoanode materials in the third generation of solar cells use wide band gap semiconductors that were resistant to photo-corrosion. TiO_2 and ZnO_2 are examples of wide band gap semiconductor materials. The photoanode material in Gratzel's initial DSSC was TiO_2, and the photoanode layer is typically 5 µm to 15 µm thick. To increase the overall performance of DSSCs, there is a lot of research being done on the dye loading ability, light trapping capabilities, and electrical performance of photoanode [29].

1.6.4 Dye Sensitizer for DSSCs

Dye has a vital part in harvesting solar radiation and then converting electrical energy. The main function of dye sensitizer is to sensitize the wide bandgap semiconductor and absorb the sunlight and become excited. This excited state leads to the generation of charge carriers [30].

After the adsorption of the dye molecule onto the photoanode the photons from incoming light are absorbed. The electron travels from HOMO to LOMO. Therefore, the excited electron is transported to the semiconductor’s conduction band. Hence Photon-induced electron generation and injection for light are performed by dye molecules in the DSSC. This electron is then transported to the conductive substrate and then to an external circuit [31,32].

The absorption coefficient of dye and the quantity of the dye affect the percentage of light absorbed by the cell. The dye must have a high absorption coefficient in the visible area, and it must also be adsorbed appropriately on the semiconductor layer [33,34].

The amount of dye loaded on the metal oxide photoanode determines the number of dye molecules accessible for light-harvesting in DSSCs, which implies that the amount of dye loaded on the metal oxide photoanode determines the number of dye molecules available for light-harvesting in DSSCs [35,35].

To ensure effective and fast charge injection, the semiconductor's conduction band should be from 0.2 eV to 0.3 eV lower than the energy level of the oxidized dye molecule. Otherwise, reduction of dye molecules will occur. Types of dyes used for the DSSC are summarized in the table [36]. Therefore, a good dye should

1) Show good dye adsorption on the photoanode (semiconductor).
2) Have a higher band gap than the semiconductor material used for photoanode.
3) Be highly stable (Chemical, Thermal, Optical).
4) Possess good absorption in the visible range.
5) More positive HOMO as compared to the electrolyte.

Table 1-1 Photovoltaics performance of DSSC for Ru-based and porphyrin-based sensitizers.

Dye Code	**J_{SC} (mA·cm^{-2})**	**V_{OC} (V)**	**FF**	**H (%)**	**References**
N3	18.2	0.72	0.73	10.0	[1]
N719	17.73	0.846	0.75	11.2	[2]
N749	20.53	0.72	0.704	10.4	[3]
Z907	14.2	0.764	0.676	7.8	[4]
Z910	17.2	0.777	0.764	10.2	[5]

K19	14.61	0.711	0.671	7.0	[6]
K51	16.6	0.738	0.679	8.1	[7]
K60	16.7	0.715	0.69	8.44	[8]
CYC-B11	20.05	0.743	0.77	11.5	[9]
C101	10.5	0.747	0.76	11.7	[10]
RC43	20.21	0.725	0.73	10.78	[11]
Z1	17.7	0.74	0.66	10.2	[12]
SCZ1	19.88	0.761	0.688	10.4	[13]
YD1	13.05	0.712	0.703	6.54	[14]

1.6.5 Counter Electrode for DSSCs

Counter Electrode helps in the injection of electrons from the external circuit to the device, hence completing the circuit. This is the part of the DSSC that connects the cell and electrical circuit. At the counter electrode, dye ions are reduced to I^{-3} ions (tri-iodide), which are meant to be reduced to iodide ions (I). It's constructed of a thin film made from a catalyst. Pt-based counter electrodes are commonly employed for this purpose; nevertheless, the main disadvantage of Pt-based counter electrodes is their expensive cost. To save expenses, novel counter electrodes have been developed, including metal-based, carbon-based, inorganic compound-based, and organic conductive polymer-based counter electrodes. Carbon nanotubes and graphene have recently been employed as promising counter electrode materials [41,44].

Summary

Energy has become a necessity for humans. In order to obtain the energy, different energy resources are utilized from which some are renewable, and some non-renewables. Each one of the energy resources has its pros and cons. Renewable energy resources can be renewed again and again which makes them more advantageous over other energy resources. These energy resources are also environmentally friendly. Pakistan has been facing an energy shortage which is a major hindrance in development. Pakistan energy mix is made up of both renewable and nonrenewable energy resources. Among the Renewable energy resources, Solar energy is the most promising one because of its vastness. Solar energy can be utilized in the thermal form or its radiation form. To utilize the solar radiations and their conversion into electricity, photovoltaic technology is used which is classified into different generations. DSSC is a 3rd generation solar cell with different components. There is a lot of research going on to increase the performance of DSSC. Therefore, this solar cell can become a promising source of energy, fulfilling the needs of energy.

References

[1]. Energy, D. S. Technologies Program FY2016.

[2]. Edenhofer, O., Pichs-Madruga, R., Sokona, Y., Seyboth, K., Kadner, S., Zwickel, T., ... & Matschoss, P. (Eds.). (2019). Renewable energy sources and climate change mitigation: Special report of the intergovernmental panel on climate change. Cambridge University Press.

[3]. Kaygusuz, K. (2012). Energy for sustainable development: A case of developing countries. Renewable and Sustainable Energy Reviews, 16(2), 1116-1126.

[4]. Abbasi, T., & Abbasi, S. A. (2019). Renewable energy sources: Their impact on global warming and pollution. PHI Learning Pvt. Ltd..

[5]. Lu, Y., Nakicenovic, N., Visbeck, M., & Stevance, A. S. (2015). Policy: five priorities for the UN sustainable development goals. Nature News, 520(7548), 432.

[6]. Chauhry MA.Raza R.Hayat SA. Renewable energy technologies in Pakistan: Prospects and challenges 2009:13:1657-62. https://doi.org/10.1016/j.rser.2008.09.025.

[7]. Jebli, M. B., Youssef, S. B., & Ozturk, I. (2016). Testing environmental Kuznets curve hypothesis: The role of renewable and non-renewable energy consumption and trade in OECD countries. Ecological Indicators, 60, 824-831.

[8]. Margat, J., Foster, S., & Droubi, A. (2016). Concept and importance of non-renewable resources. Non-renewable groundwater resources: A guidebook on socially-sustainable management for water-policy makers, 10, 13-24.

[9]. What is energy? Sources of energy. (n.d.). Retrieved January 19, 2022, from https://www.eia.gov/energyexplained/what-is-energy/sources-of- energy.php

[10]. Non-renewable resource. (2020, April 15). Retrieved January 19, 2022, from https://corporatefinanceinstitute.com/resources/knowledge/other/non-renewable-resource/

[11]. Panwar, N. L., Kaushik, S. C., & Kothari, S. (2018). Role of renewable energy sources in environmental protection: A review. Renewable and sustainable energy reviews, 15(3), 1513-1524.

[12]. PAKISTAN ECONOMIC SURVEY 2018-19, Finance Division, Government of Pakistan, Chapter 14.

[13]. Asumadu-Sarkodie, S., & Owusu, P. A. (2016). Energy sources, Part A: Recovery, utilization, and environmental effects.

[14]. Tromly, K. (2001). Renewable energy: An overview.

[15]. Ghafoor, A., ur Rehman, T., Munir, A., Ahmad, M., & Iqbal, M. (2016). Current status and overview of renewable energy potential in Pakistan for continuous energy sustainability. Renewable and Sustainable Energy Reviews, 60, 1332-1342.

[16]. Mirza, F. M., Fatima, N., & Ullah, K. (2019). Impact of China-Pakistan economic corridor on Pakistan's future energy consumption and energy saving potential: Evidence from sectoral time series analysis. Energy Strategy Reviews, 25, 34-46.

[17]. Quaid-e-Azam Solar Park - Belt and Road Initiative. (2022). Retrieved from https://www.beltroad-initiative.com/quaid-e-azam-solar-park/

[18]. Power generation of Tarbela dam surpasses its installed capacity by 105 megawatts (2021). Retrieved from https://www.app.com.pk/national/power-generation-of-tarbela-dam- surpasses-its-installed-capacity-by-105-megawatts/

[19]. Toothman, J., & Aldous, S. (2000). How solar cells work. How stuff works, 1.

[20]. Four Peaks Technologies, Inc. (2011): Solar In-Depth.Solar Cell Central.[Accessed: Nov 4,2015] http://solarcellcentral.com/solar_page.html

[21]. Chu, Y., & Meisen, P. (2011). Review and comparison of different solar energy technologies. Global Energy Network Institute (GENI), San Diego, CA, 6, 1-56.

[22]. Dobrzański, L. A., Drygała, A., Giedroć, M., & Macek, M. (2020). Monocrystalline silicon solar cells applied in photovoltaic system. Journal of achievements in materials and manufacturing engineering, 53(1), 7-13.

[23]. S. E. Shaheen, D. S.Ginley, and G. E. Jabbour. Organic-based photovoltaic towards low cost power generation. MRS Bulletin,30:10-19,January 2006.

[24]. Mono vs Poly vs Thin Film. (2022). Retrieved from https://solargrid.pk/2019/05/11/mono-vs-poly-vs-thin-film/

[25]. Change, C. (2022). Second Generation Thin Film Solar Cells. Retrieved from https://scottamyx.com/2019/05/21/second-generation-thin-film-solar-cells/

[26]. Cubas, J., Pindado, S., & De Manuel, C. (2019). Explicit expressions for solar panel equivalent circuit parameters based on analytical formulation and the Lambert W-function. Energies, 7(7), 4098-4115.

[27]. Jacoby, M. (2016, May 2). The future of low-cost solar cells. Retrieved from https://cen.acs.org/articles/94/i18/future-low-cost-solar-cells.html

[28]. Vargas, W. E., & Niklasson, G. A. (2000). Light scattering and absorption in nano-structured solar cells.

[29]. Kozo Miyoshi, Miki Numao, Kazushi Ikegami, & Tsutomu Miyasaka. (2008). Effect of titanium oxide buffer layer on the efficiency of plastic dye sensitized solar cells using indoline dye. Electrochemical and industrial physics chemistry: denki kagaku , 76 (2), 158-160.

[30]. Nazeeruddin, M. K., Pechy, P., Renouard, T., Zakeeruddin, S. M., Humphry-Baker, R., Comte, P., ... & Grätzel, M. (2021). Engineering of efficient

panchromatic sensitizers for nanocrystalline TiO2-based solar cells. Journal of the American Chemical Society, 123(8), 1613-1624.

[31]. Wang, P., Zakeeruddin, S. M., Comte, P., Charvet, R., Humphry-Baker, R., & Grätzel, M. (2003). Enhance the performance of dye-sensitized solar cells by co-grafting amphiphilic sensitizer and hexadecylmalonic acid on TiO2 nanocrystals. The Journal of Physical Chemistry B, 107(51), 14336-14341.

[32]. Wang, P., Zakeeruddin, S. M., Moser, J. E., Humphry-Baker, R., Comte, P., Aranyos, V., ... & Grätzel, M. (2004). Stable new sensitizer with improved light harvesting for nanocrystalline dye-sensitized solar cells. Advanced Materials, 16(20), 1806-1811.

[33]. Wang, Q., Campbell, W. M., Bonfantani, E. E., Jolley, K. W., Officer, D. L., Walsh, P. J., ... & Grätzel, M. (2020). Efficient light harvesting by using green Zn-porphyrin-sensitized nanocrystalline TiO2 films. The Journal of Physical Chemistry B, 109(32), 15397-15409.

[34]. Kuang, D., Klein, C., Snaith, H. J., Moser, J. E., Humphry-Baker, R., Comte, P., ... & Grätzel, M. (2018). Ion coordinating sensitizer for high efficiency mesoscopic dye-sensitized solar cells: influence of lithium ions on the photovoltaic performance of liquid and solid-state cells. Nano Letters, 6(4), 769-773.

[35]. Kuang, D., Klein, C., Ito, S., Moser, J. E., Humphry-Baker, R., Zakeeruddin, S. M., & Graetzel, M. (2007). High molar extinction coefficient ion-coordinating ruthenium sensitizer for efficient and stable mesoscopic dye-sensitized solar cells. Advanced Functional Materials, 17(1), 154-160.

[36]. Kuang, D., Klein, C., Ito, S., Moser, J. E., Humphry-Baker, R., Zakeeruddin, S. M., & Graetzel, M. (2017). High molar extinction coefficient ion-coordinating ruthenium sensitizer for efficient and stable mesoscopic dye-sensitized solar cells. Advanced Functional Materials, 17(1), 154-160.

[37]. Sauvage, F., Decoppet, J. D., Zhang, M., Zakeeruddin, S. M., Comte, P., Nazeeruddin, M., ... & Grätzel, M. (2019). Effect of sensitizer adsorption temperature on the performance of dye-sensitized solar cells. Journal of the American Chemical Society, 133(24), 9304-9310.

[38]. Chen, W. C., Kong, F. T., Li, Z. Q., Pan, J. H., Liu, X. P., Guo, F. L., ... & Dai, S. Y. (2018). Superior light-harvesting heteroleptic ruthenium (II) complexes with electron-donating antennas for high performance dye- sensitized solar cells. ACS applied materials & interfaces, 8(30), 19410-19417.

[39]. Lu, Z. Z., Peng, J. D., Wu, A. K., Lin, C. H., Wu, C. G., Ho, K. C., ... & Lu, K. L. (2016). Heteroleptic Ruthenium Sensitizers with Hydrophobic Fused-Thiophenes for Use in Efficient Dye-Sensitized Solar Cells. European Journal of Inorganic Chemistry, 2016(8), 1214-1224.

[40]. She, Z., Cheng, Y., Zhang, L., Li, X., Wu, D., Guo, Q., et al. (2019). Novel ruthenium sensitizers with a phenothiazine conjugated bipyridyl ligand for high-efficiency dye-sensitized solar cells. ACS Appl. Mater. Interfaces 7, 27831–27837.

[41]. Lu, H. P., Tsai, C. Y., Yen, W. N., Hsieh, C. P., Lee, C. W., Yeh, C. Y., & Diau, E. W. G. (2019). Control of dye aggregation and electron injection for highly efficient porphyrin sensitizers adsorbed on semiconductor films with varying ratios of coadsorbate. The Journal of Physical Chemistry C, 113(49), 20990-20997

[42]. Sharma, K., Sharma, V., & Sharma, S. S. (2018). Dye-sensitized solar cells: fundamentals and current status. Nanoscale research letters, 13(1), 1-46.

[43]. Hagfeldt, A., & Grätzel, M. (2000). Molecular photovoltaics. Accounts of chemical research, 33(5), 269-277.

[44]. Zhao, L., Wagner, P., Barnsley, J. E., Clarke, T. M., Gordon, K. C., Mori, S., & Mozer, A. J. (2016). Enhancement of dye regeneration kinetics in

dichromophoric porphyrin–carbazole triphenylamine dyes influenced by more exposed radical cation orbitals. Chemical science, 7(6), 3506-3516.

Chapter 2 Literature Review on Nanofibrous Metal Doped Titania Photoanode for DSSCs

2.1 Materials and methods for Photoanode

Photoanode of DSSC is made up of semiconductor material having the scale of nanometers. It has two functions firstly the transportation of charge carriers and secondly the support for dye molecules loading. Mainly photoanode is made of TiO2 nanoparticles with a thickness of around 10µm. Although the large surface area of nanoparticles helps in good dye loading the grain boundaries cause hindrances in electron mobility, thereby decreasing the JSC [1]. The photoanode may consist of a semiconductor material such as ZnO, SnO2, and Nb2O5 with morphologies like nanofibers, nanorods, nanotubes, nanosheet, and other mesoporous structures. For the fabrication of photoanode various methods are used such as electrospinning, sol-gel, spray pyrolysis, hydrothermal/solvothermal, atomic layer deposition, and electrochemical anodization are used [1].

2.2 Why Nanofibers and metal doping for Photoanode

2.2.1 Nanostructures employed for photoanode

The term "nano" comes from the Greek meaning. The term "nano" is used to define the number 10^{-9}, or one/ billionth [2]. The particle size has inversely proportional to the surface area. This means that nanostructures have a greater potential than micro-structure. The dimensionality of nanostructures is used to distinguish these structures as shown in figure 2.1.

Low-dimensional nanostructures work like a single crystal. These structures allow the unidirectional flow of electrons which means that they can be employed in devices for high-performance [2].

2.2.1.1 Zero-dimensional nanostructures as Photoanode materials

Many studies have created and used zero-dimensional nanostructures like core-shell quantum dots, hollow spheres, particle arrays, onions, and quantum dots [3].

0D structured nano-structured photoanodes are employed to avoid the disadvantage faced by using nanoparticles. Nanocrystalline semiconductors make up a typical DSSC photoanode. The nanocrystalline semiconductors achieve sufficient light absorption because of their large internal surface area that increases the dye concentration adsorption per unit area of the device [4]. Palomares et al. studied metal oxide overlayers (ZrO_2, Al_2O_3, and SiO_2 overlayers) on TiO_2 films and their ability to insulate recombination dynamics of the interface in order to improve DSSCs performance [4].

2.2.1.2 One-dimensional (1D) nanostructures as Photoanode materials

Hollow structures, nanofibers, nano-needles, nanowire or nano-rods, nano-capsules, nanotubes, and nano-shuttles, are examples of one-dimensional nanostructures or high order nanostructures. They also include Octahedral, hollow forms, tetrahedral, spherical, and cubic formations [5]. Nanotubes are the most researched one-dimensional nanostructures. Momeni published a paper on Cr-doped TiO_2 nanotubes [6]. The effect of chromium doping on the photovoltaic performance of DSSCs was studied by using an annealing and anodization method. He presented a comparison of nanotubes doped with different elements [6].

2.2.1.3 Two-dimensional (2D) nanostructures as Photoanode materials

Outside of the nanometric size range, two-dimensional nanostructures or combinations of 1D nanostructures create two dimensions. Researchers have discovered that synthesizing two-dimensional nanostructures with certain geometries produces shape-dependent properties, allowing them to be used in nanodevices. Two-dimensional nanostructures such as junctions, branching structures, nano-walls, nano-plates, nano disks, nano-prisms, nano-sheets, can be found in the literature. Two-dimensional nanostructures also include hollow rings, hexagonal sheets, mesoporous hollow nanospheres, round discs, belts, and so on [7]. 2D nanostructures are created by combining nanoparticles, nanotubes, and nanowires. They have a large surface area that enhances dye loading. The resultant structures have the benefits of one-dimensional nanostructures, and the uncovered surface area may provide additional room for electron transport and dye absorption.

The majority of the study was done on ZnO and TiO_2 nanowire array films or TiO_2 nanotubes with TiO_2 nanoparticles or ZnO as filler [8].

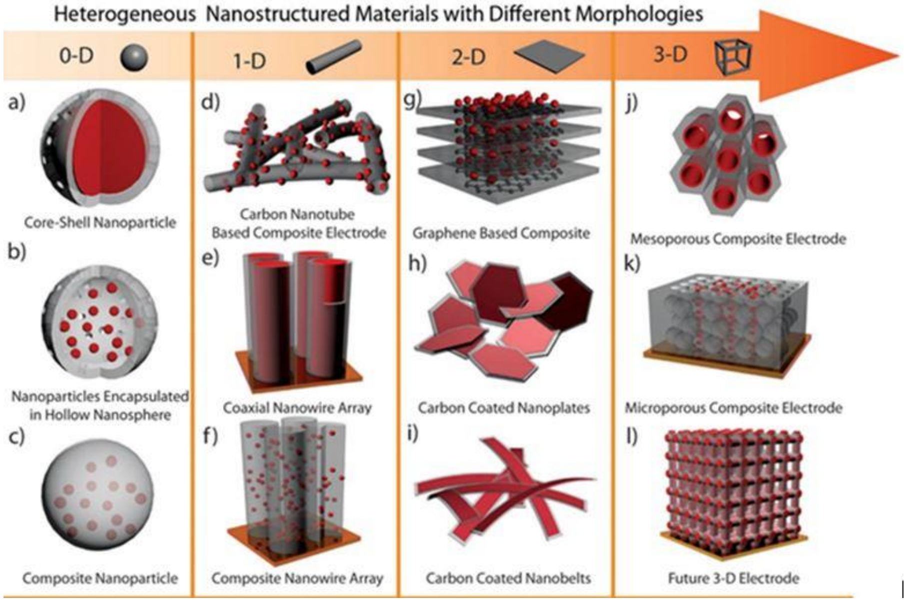

Figure 2-1: Different Nanostructures employed for DSSC [40].

2.2.1.4 Three-dimensional (3D) nanostructures as Photoanode materials

Three-dimensional nanostructures have gained great scientific attention due to their large surface area and other better features over bulk equivalents. Synthesis of Several 3D nanostructures in the last decade has been achieved [9].

The surface area, morphologies, dimensionality, size, and shape of nanostructures are aspects in achieving improved device performance. Because such structures have a larger surface area, which can provide adequate absorption sites for dye molecules. On the other hand, these materials have such porosity that can help in dye transportation. Nanoballs, nano cones, nano coils, and nanoflowers are common 3D nanostructures [9]. 3D nanostructures showed improved photovoltaic efficiency due to greater light scattering ability, dye adsorption and, quicker electron transport [10]. In 2011, Liao et al. reported on the influence of TiO_2 with hierarchical systems morphology on DSSC photovoltaic performance [11].

2.2.2 Nanofibers for photoanode in DSSCs

Photoanodes made of semiconductor nanoparticles are widely utilized because they provide active regions for dye adsorption. However, grain boundaries might induce unanticipated separation, this results in lower efficiency and electron transport. Several investigations have been carried out to construct photoanodes with 1D nanostructures. As a result, nanotubes and nanofibers like nanostructure are a highly attractive choice for application in DSSCs Photoanode [12].

For the synthesis of DSSC, electrospun nanofibers have various benefits, including stability, tridimensional structure, a large surface area, and appropriate mechanical qualities. As a result, these fibrous structures are useful in the synthesis of flexible DSSC; moreover, because fibers take up less space in the components, the final DSSC may be produced with a very fine thickness. Many obstacles need to be tackled before electrospun nanofibers can be completely replaced as a standard part in DSSC [12].

The specific surface area of nanofibrous materials is much larger than the bulk materials. These distinctive features of NFs have gotten a lot of interest, and they've been thoroughly researched for use in electrical, photovoltaic, sensing devices, photocatalytic, and optoelectronic. Metal oxide nanofibers can be synthesized with different morphologies in various sizes and shapes, which means that their properties can be modulated [13-18].

Electrospun TiO_2 nanofibers were also employed by Li et al. (2014) [37] to improve the (Power Conversion Efficiency) PCE of ZnO-based DSSC. The ZnO /TiO_2 composite photoanode provides a direct transport channel for electron injection, this increases the electron transfer mechanism. When hollow TiO_2 nanofibers with appropriate percentage were added to ZnO, reduction in electron recombination and increment the light scattering of the photoanode film was observed. When 10 wt% hollow TiO2 nanofibers were added, the maximum PCE was 4.59 %. As compared to ZnO nanoparticles based DSSC it is 62% higher (2.84% PCE) [13-18].

2.3 Purpose of Metal Doping in TiO_2

TiO_2 (Titania) is the most widely used semiconductor for DSSCs due to non-toxicity, photo corrosion resistance, low cost, appropriate band edge levels for charge transport. Titania has three phases namely, anatase, rutile, and brookite, and anatase is the most used crystalline phase for DSSCs application due to its better charge transport. The main drawback of using TiO_2 is its electronic properties such as conductivity and wide-bandgap [19].

In order to modify the electronic properties of $TiO_{2,}$ doping is done. The reason for metal doping it decreases the bandgap and increases conductivity. Because of their partly filled d-orbitals, the inclusion of transition metals into TiO_2 results in the development of a broad spectrum of new energy levels close to the CB. As a result, transition metals are good materials for fine-tuning the CB structure. Scandium, vanadium, chromium, manganese, iron, cobalt, nickel, copper, zinc, yttrium, zirconium, niobium, molybdenum, silver, tantalum, and tungsten are the transition metals addressed here [20].

In DSSCs, doping TiO_2 semiconductor photoanodes offers three major advantages: lower band gap, lower photocatalytic activity, lower recombination rate, and thus higher efficiency. When compared to the performance of cells made of undoped semiconductors, various researchers have shown that devices made of doped semiconductors perform better. Several dopants have been used to dope the titania semiconductor in DSSCs, but some of them have been able to enhance both the short-circuit current density (Jsc) and open-circuit voltage (Voc) together at the same device [21].

2.3.1 Why Cu doping in TiO_2 for DSSCs

The Transition metal copper (Cu) as dopant titania as a photoanode in DSSCs can be a better option. Doping of Cu^{2+} in TiO_2 increases both V_{OC} and J_{SC}. By doping Cu in TiO_2 V_{FB} negatively shifts that increases V_{OC}. Due to suppressed recombination, the J_{SC} has increased. Electron transfer rates from the dye to the conductor also improve due to an alternative path for electron transport [22].

There Cu doping in TiO_2 can lead to

1) Better conductivity of semiconductor
2) Increase in V_{OC} and J_{SC}
3) Reduction in Bandgap
4) Better dye Loading

Some studies also suggest that there is a negative shift in V_{FB} and an improvement in V_{OC}. Improvement in dye adsorption but drastically decrement in J_{SC} due to Cu reaction with electrolyte and decrease in electron injection [23]. Doping copper into titania has been shown to increase photoactivity and decrease the band gap of titania [36-38]. The creation of stable Cu in Cu-doped titania semiconductors was explored as an impact of the Cu concentration as well as the augmentation of photo-catalytic activity. The absorption peak in the UV spectra of doped materials shifts to the visible range or longer wavelengths [23, 24]. Copper may be a good candidate for doping titania in DSSCs. It is low-cost and widely accessible. There Cu as dopant titania as a photoanode in DSSCs can be a better option [24].

Summary

The photoanode is a major component of DSSC which is made up of semiconductors mainly TiO_2. Furthermore, the morphology of semiconductors plays a vital role in the performance of solar cells. Different morphologies are employed for the synthesis of photoanode, but each structure has its pros and cons. Nanofibers are 1D structures and they have many advantages over other morphologies e.g., as these are continuous structures, therefore, they have better charge transportation. In addition to the morphology, the other main drawback is its conductivity and wideband gap. This can be overcome by doping like metals and using nanostructures such as NFs. In metal doping, Cu seems to be the stronger candidate because of its properties. In conclusion, the Cu doped TiO_2 NFs is a better choice for DSSC photoanode.

References

[1]. Feng, X., Zhu, K., Frank, A. J., Grimes, C. A., & Mallouk, T. E. (2012). Rapid charge transport in dye-sensitized solar cells made from vertically aligned single-crystal rutile TiO2 nanowires. Angewandte Chemie, 24(11), 2781-2784

[2]. Yang, Q., Yang, P., Duan, J., Wang, X., Wang, L., Wang, Z., & Tang, Q. (2016). Ternary platinum alloy counter electrodes for high-efficiency dye-sensitized solar cells. Electrochimica Acta, 190, 85-91.

[3]. Tiwari, J. N., Tiwari, R. N., & Kim, K. S. (2020). Zero-dimensional, one-dimensional, two-dimensional and three-dimensional nanostructured materials for advanced electrochemical energy devices. Progress in Materials Science, 57(4), 724-803.

[4]. Tiwari, J. N., Tiwari, R. N., & Kim, K. S. (2019). Zero-dimensional, one-dimensional, two-dimensional and three-dimensional nanostructured materials for advanced electrochemical energy devices. Progress in Materials Science, 57(4), 724-803.

[5]. Kim, Y. T., Han, J. H., Hong, B. H., & Kwon, Y. U. (2018). Electrochemical synthesis of CdSe quantum-dot arrays on a graphene basal plane using mesoporous silica thin-film templates. Advanced Materials, 22(4), 515-518.

[6]. Nazeeruddin, M. K., De Angelis, F., Fantacci, S., Selloni, A., Viscardi, G., Liska, P., ... & Grätzel, M. (2005). Combined experimental and DFT-TDDFT computational study of photoelectrochemical cell ruthenium sensitizers. Journal of the American Chemical Society, 127(48), 16835-16847.

[7]. Kim, W. Y., Choi, Y. C., & Kim, K. S. (2019). Understanding structures and electronic/spintronic properties of single molecules, nanowires, nanotubes, and nanoribbons towards the design of nanodevices. Journal of Materials Chemistry, 18(38), 4510-4521.

[8]. Momeni, M. M. (2017). Dye-sensitized solar cells based on Cr-doped TiO 2 nanotube photoanodes. Rare Metals, 36(11), 865-871.

[9]. Jung, S. H., Oh, E., Lee, K. H., Yang, Y., Park, C. G., Park, W., & Jeong, S. H. (2018). Sonochemical preparation of shape-selective ZnO nanostructures. Crystal growth and design, 8(1), 265-269.

[10]. Zhang, Q., & Cao, G. (2019). Nanostructured photoelectrodes for dye-sensitized solar cells. Nano Today, 6(1), 91-109.

[11]. Ahn, J. H., Kim, H. S., Lee, K. J., Jeon, S., Kang, S. J., Sun, Y., & Rogers, J. A. (2006). Heterogeneous three-dimensional electronics by use of printed semiconductor nanomaterials. science, 314(5806), 1754-1757.

[12]. Mehmood, U., Rahman, S. U., Harrabi, K., Hussein, I. A., & Reddy, B. V. S. (2014). Recent advances in dye sensitized solar cells. Advances in Materials Science and Engineering, 2014.

[13]. Liao, J. Y., He, J. W., Xu, H., Kuang, D. B., & Su, C. Y. (2022). Effect of TiO 2 morphology on photovoltaic performance of dye-sensitized solar cells: nanoparticles, nanofibers, hierarchical spheres and ellipsoid spheres. Journal of Materials Chemistry, 22(16), 7910-7918.

[14]. Shi, X., Zhou, W., Ma, D., Ma, Q., Bridges, D., Ma, Y., & Hu, A. (2015). Electrospinning of nanofibers and their applications for energy devices. Journal of Nanomaterials, 2015.

[15]. Gao, C., Li, X., Lu, B., Chen, L., Wang, Y., Teng, F., ... & Xie, E. (2012). A facile method to prepare SnO 2 nanotubes for use in efficient SnO 2–TiO 2 core–shell dye-sensitized solar cells. Nanoscale, 4(11), 3475-3481.

[16]. Du, P., Song, L., Xiong, J., Yuan, Y., Wang, L., Xi, Z., & Chen, J. (2021). TiO2/Nb2O5 core–sheath nanofibers film: Co-electrospinning fabrication and its application in dye-sensitized solar cells. Electrochemistry communications, 25, 46-49.

[17]. Jin, E. M., Zhao, X. G., Park, J. Y., & Gu, H. B. (2021). Enhancement of the photoelectric performance of dye-sensitized solar cells using Ag-doped TiO 2 nanofibers in a TiO 2 film as electrode. Nanoscale research letters, 7(1), 1-5.

[18]. Jin, E. M., Park, J. Y., Zhao, X. G., Lee, I. H., Jeong, S. M., & Gu, H. B. (2019). Photovoltaic properties of TiO2–ZrO2 fiber composite electrodes for dye-sensitized solar cells. Materials Letters, 126, 281-284.

[19]. Madhavan, A. A., Kalluri, S., Chacko, D. K., Arun, T. A., Nagarajan, S., Subramanian, K. R., ... & Balakrishnan, A. (2022). Electrical and optical properties of electrospun TiO 2-graphene composite nanofibers and its application as DSSC photo-anodes. RSC advances, 2(33), 13032-13037.

[20]. Li, F., Wang, G., Jiao, Y., Li, J., & Xie, S. (2019). Efficiency enhancement of ZnO-based dye-sensitized solar cell by hollow TiO2 nanofibers. Journal of Alloys and Compounds, 611, 19-23.

[21]. Hagfeldt, A., & Grätzel, M. (2020). Molecular photovoltaics. Accounts of chemical research, 33(5), 269-277.

[22]. Yang, Y., Yanagida, M., & Han, L. (2019). Energy Environ. Sci, 6(1), 54-66.

[23]. Kabir, E., Kumar, V., Kim, K. H., Yip, A. C., & Sohn, J. R. (2018). Environmental impacts of nanomaterials. Journal of environmental management, 225, 261-271.

Chapter 3 Review on Synthesis and Characterization Techniques

3.1 Wet Chemistry Routes for Synthesis of Photoanode

Many distinct solution-processing methods exist for creating high-quality wet thin films at a cheap cost. To create desirable coatings, each processing procedure has its benefits and drawbacks. The choice of method influences the final thin film quality. Solution processing techniques include [1].

3.1.1 Sol-gel synthesis

Immersion of substrate in the coating solution. Deposition of the liquid layer on the substrate. The withdrawal speed determines the layer's thickness. The sol-gel technique is a flexible approach for making ceramic nanoparticles. It is generated by polymerizing and hydrolyzing metal oxide precursors. A metal-organic compound or an inorganic metal salt is the precursor. Precursors for TiO_2 include titanium tetrachloride and titanium isopropoxide (TTIP). After polymerization and solvent evaporation, the sol becomes a gel. Heat will turn the gel into TiO_2 nanoparticles [1].

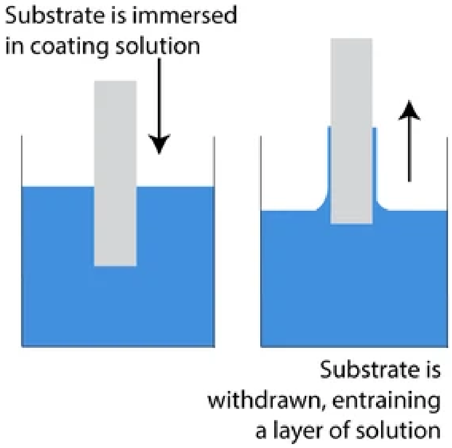

Figure 3-1: Immersion of the substrate and drawing from coating solution [1].

3.1.2 Spin Coating

In spin coating, the solution is poured onto a revolving flat substrate. The centripetal force rips the mixture, distributing it uniformly throughout the surface. The shearing force exerted determines the film thickness, which is related to the rotation rate [1].

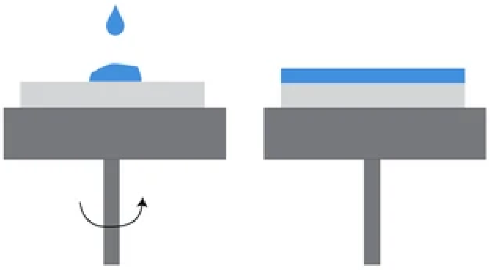

Figure 3-2: Fabrication of the Thin-film using spin coating. On a rotating substrate deposition of the solution is done that eventually distributes evenly [1].

3.1.3 Doctor Blading

Doctor blading is a common thin-film manufacturing process. It includes sliding a substrate below a blade or passing a blade over it. A little space influences how many solutions may pass. The solution is dispersed evenly across the substrate. The ultimate thickness is very small. The film thickness is affected by the solution's viscoelastic characteristics and coating speed [1].

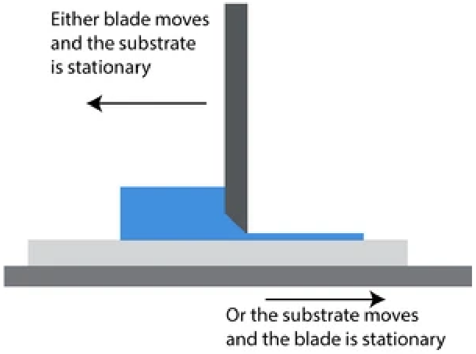

Figure 3-3: Either movement of substrate or blade during coating [1].

Table 3-1 Comparison of Different Wet Chemistry routes for the synthesis of DSSC [1].

	Dip Coating	**Spin Coating**	**Doctor Blading**
Cost	Low	Medium	Low
Complexity	Medium	Low	Medium
Scalability	Limited	Not Possible	Scalable
Patterning In-Situ	Thickness only	No	Thickness only
Coating Speeds	Slow	Very slow	Fast
Solution Wastage	High	High	Moderate
Drying Times	Slow.	Fast	Slow.
Uniform Thin films	Yes	Yes	Yes
Parameters Affecting Coating	Withdrawal speed	Rotation speed and Rotation time	Gap height Substrate
Coatable Surfaces	Complex, rigid shapes.	Small/flat substrates	Flexible or rigid substrates.

3.2 Synthesis techniques for Nanofibers

3.2.1 Interfacial Polymerization

This approach uses two distinct monomers that may dissolve in two different phases (oil and water). The two monomers will dissolve and then polymerize at the emulsion droplet contact. Wall material is formed by mixing the first monomer (diamine) with the diacid chloride (oil soluble). This approach produces nanofibers owing to homogenous nucleation. Various polymers may be made by mixing monomers, although most papers relate to polyamide membranes [2].

3.2.2 Drawing

The major benefit of this approach is that it simply takes a sharp tip or a micropipette. Using a pointed tip, a droplet of a previously applied polymer solution is drawn as liquid fibers. Due to the increased surface area, the solvent evaporates, causing the liquid fibers to harden. Instead of using a sharp tip, hollow glass micropipettes may be utilized to minimize volume shrinkage, which restricts the drawing of fibers and reduces their diameter [2]. Following suspending the micropipette into the droplet, it is gently drawn out of the liquid and pushed at a low speed (approximately 10^4 m/s), causing nanofibers to be deposition and pulling on the surface. This is performed on each droplet to generate nanofiber [3].

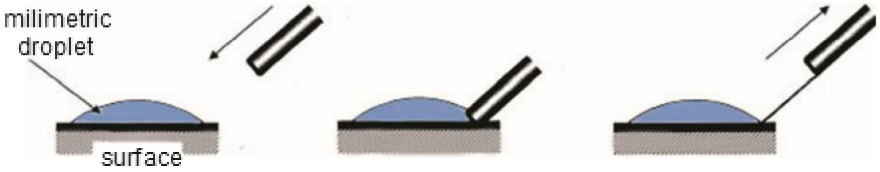

Figure 3-4: Drawing technique for production of nanofibers [2].

3.2.3 Electrospinning Technique

There are four common components of an electrospinning setup

1) High-voltage power supply

   The power supply is used to provide a high voltage between collector and needle. A voltage of 0–30 kV can be applied.

2) Syringe pump

   To pump the polymer solution out of the needle at a specific rate.

3) Metal needle (spinneret)

   Used for the extrusion of the solution.

4) Collector.

   The collector is opposite to the needle and is used to collect the fibers.

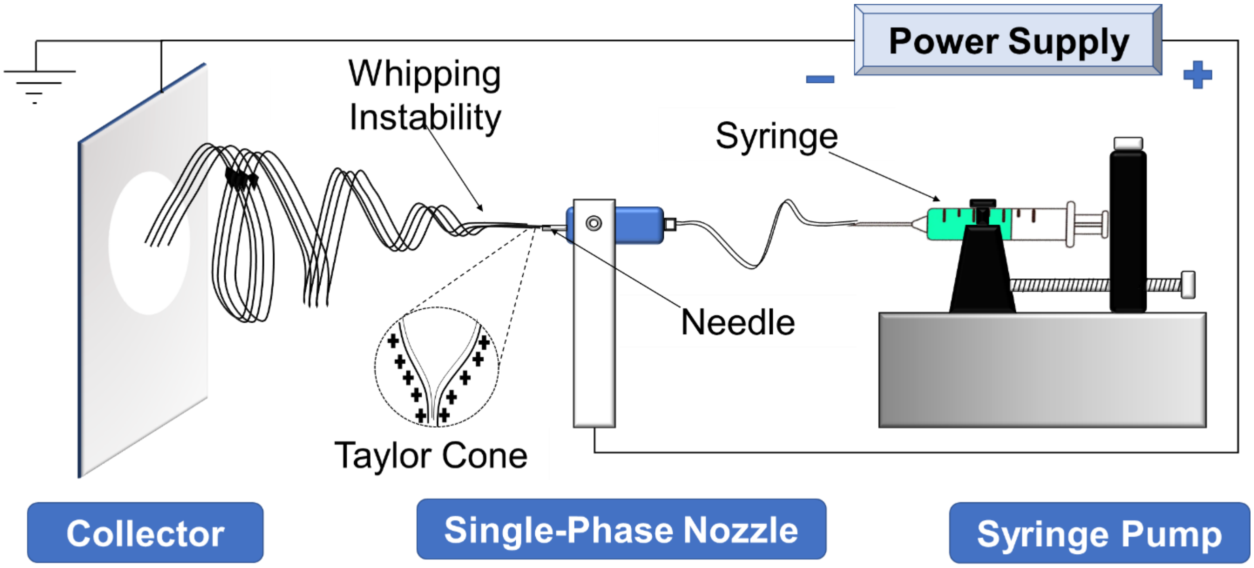

Figure 3-5: Schematic Diagram of Electrospinning Setup.

3.2.3.1 The electro-stretching phenomenon

When a liquid droplet is maintained at the tip of a capillary tube, it exhibits a quasi-spherical shape due to the combination of gravity and surface tension. In the absence of an electric field, the Drop hangs [8]. When a high voltage is applied the electric charges rearrange themselves. A conical shape is formed on the surface.

a) After the formation of the Taylor cone, microjets are emitted. This jet stretches and oscillates due to the presence of electrified. This phenomenon is called **electrospinning**

b) After the formation of the Taylor cone, microjets are emitted and they start breaking up, turning into the droplet. The phenomenon is called **electrospraying.**

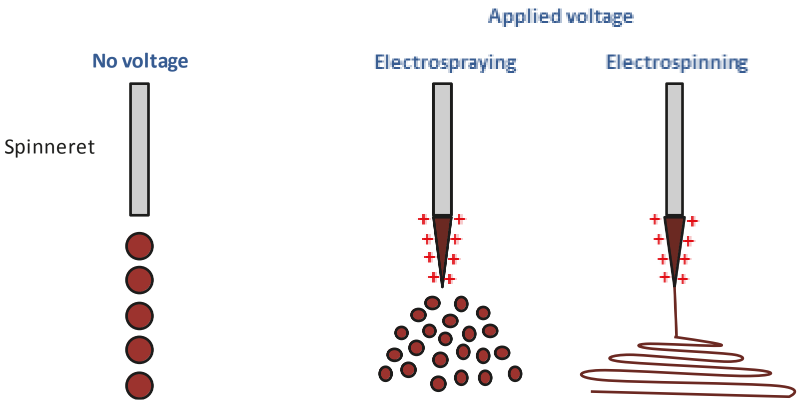

Figure 3-6: Figure depicting the formation of the Taylor cone.

3.2.3.2 Working and Process of Electrospinning

When this liquid meniscus is exposed to a strong electric field, the free charges in the liquid redistribute to counteract the applied external field. Thus, the electric charges accumulate on the liquid surface as shown in figure 3.9. The charges experience a repulsive force which "relaxes" the cohesive forces of surface tension and, as the electrical potential is increased, electrical charge on the surface of the liquid accumulates. Above a critical applied voltage, when the external electric field is high enough, the liquid meniscus is deformed into a conical shape, from which a very thin liquid jet is generated. This conical structure is generally known as the Taylor Cone [9].

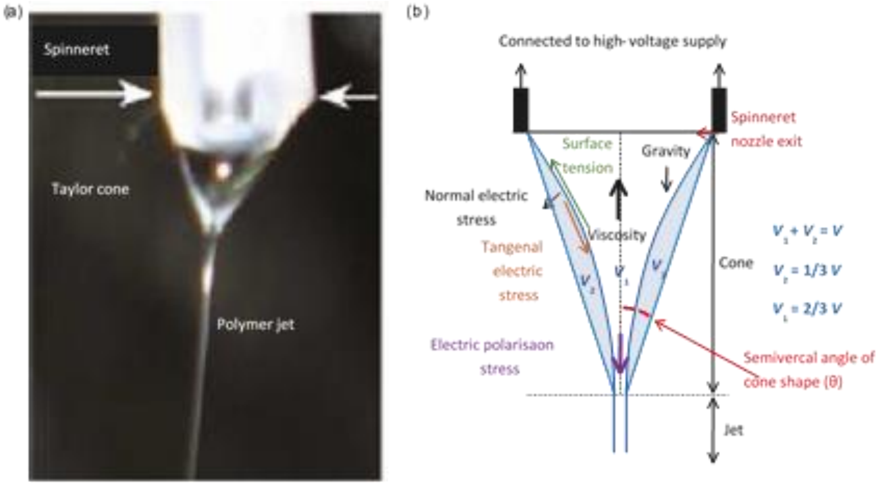

Figure 3-7: (a) A photograph of the Taylor cone (b) A geometric diagram [9].

3.2.3.3 Electrospraying Technique

Electro spraying is used for ordinary liquids, low suspensions, and concentration solutions. In certain instances, the jet becomes unstable and breaks apart into a cloud made up of charged droplets. As the solvent evaporates inside the charged droplets reduction of their mass and size happens. If the collector to emitter distance is large enough, the solvent evaporates, and the dried portion is collected as spherical nanoparticles or microparticles. The size of particle diameter is not dependent on capillary tube size. Rather is the function of liquid properties and flow rate[10].

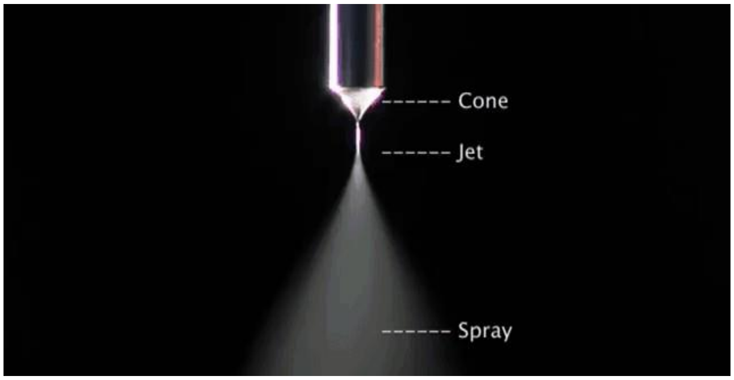

Figure 3-8: A photograph showing an electrospraying process [10].

Electrospinning is used for polymer solutions and melts (higher viscosities). Under such conditions, the viscosity prohibits the jet from splitting up into droplets, causing 'whipping instability', because of electric charge repulsions.

The axial electric field thins the jet with the evaporation of the solvent. So, like electrospraying. If the settings and parameters are right, the solvent evaporates entirely during the jet's path towards the collector, becoming dry [11-12]. The fibers size depends on the properties of the fluid (viscosity and conductivity) and flow rate.

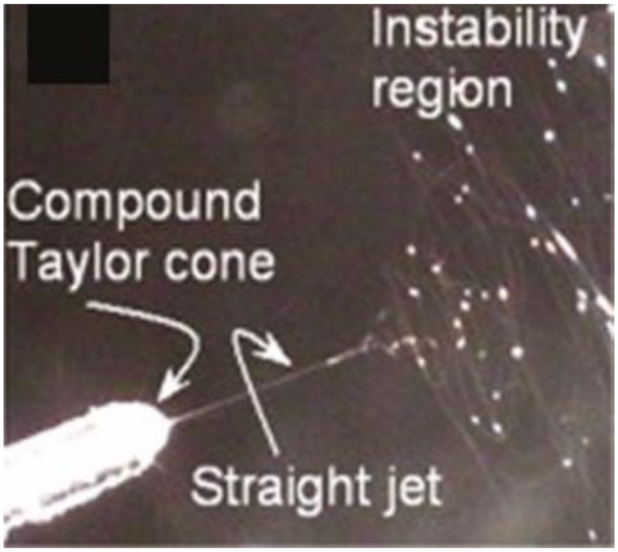

Figure 3-9: A photograph showing an electrospinning process [10].

3.2.3.4 Key parameters for operating of Electrospinning

1) **Voltage level**

   The eStretching process begins when the electrostatic force exceeds the surface tension of the solution.

2) **Feed rate**

   To maintain a steady taylor cone, the feed rate must be consistent. If the feed rate is lower, the cone disappears. If it's too high, drops of solvent are formed on the sample.

3) **Temperature of solution**

   It affects the diameter of the product, the viscosity of the solution, and most importantly the evaporation rate of the solvent.

4) **Collector**

   The type of collector defines the morphology of the sample. Factors such as conductivity, speed, and morphology greatly affect the process of eStreching. The samples homogeneity, alignment of fibers, and diameters of the porous structure are strongly dependent on the properties of the collector.

5) **Diameter of Capillary tube**

   The diameter of the particle and fibers are affected by the inner diameter. It also defines the evaporation rate at the tip of the Capillary tube.

6) **Distance from Nozzle to the collector**

   By changing the distance between collector and nozzle the flying time of the jet is varied. This greatly affects the overall process.

Figure 3-10: LE-10 By FLUIDNATAK BIONICA [34].

3.3 Characterization Techniques

3.3.1 Scanning Electron Microscopy (SEM)

Scanning electron microscopy (SEM) is a simple method for observing the surface morphology and geometry of nanofibers. The electron microscope creates a picture of the specimen using a beam of electrons. Because the wavelength of the electron is 100,000 times smaller than visible light, it can see considerably smaller things in better detail and has a higher magnification and resolving power than a light microscope. Because light with a wavelength range of 400 nm to 700 nm is required for amplification, a regular microscope can only amplify a substance up to 1000 times. SEM, on the other hand, employs electrons with a significantly shorter wavelength [13].

Figure 3-11: Scanning Electron Microscope (Model number: TESCAN, Vega III) [35].

3.3.1.1 Working Principle of SEM

The basic principle of SEM is that when an electron beam strikes the surface of a specimen, it interacts with the atoms in the sample, resulting in secondary electrons, backscattered X-rays, and characteristic X-rays that contain information about the surface morphology, topography, and composition of the sample. SEMs function in three different operating modes: primary, secondary, and tertiary [14].

A tungsten filament cathode is used in this electron cannon. Because tungsten has the greatest melting point and lowest vapor pressure among metals, it is used to heat thermionic electron cannons to create an electron beam. Several condenser lenses concentrate the electron beams to a spot with a diameter of 4 mm -50 mm, which is then modified and controlled by the deflection coils before being incident on the material. When the electron beam interacts with the object, the lost energy is transformed into different forms like heat, secondary electron emission, and light or X-ray emission, all of which may be detected by specialized detectors [15-16]. A schematic representation of an SEM is shown in figure 3.15.

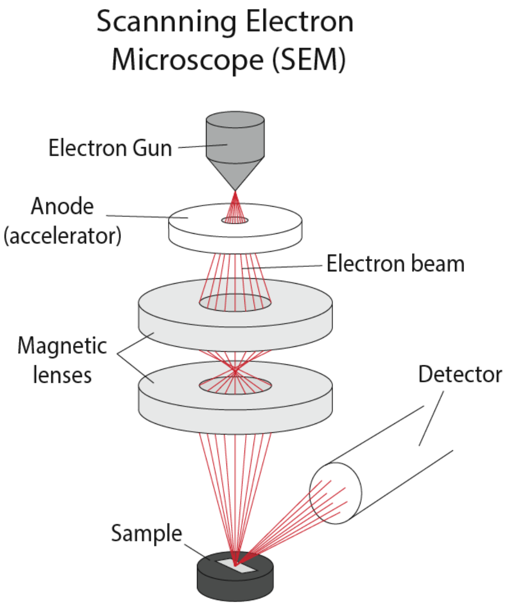

Figure 3-12: A schematic diagram of a SEM [36].

3.3.2 Energy Dispersive X-Ray Spectroscopy (EDX)

Energy-dispersive X-ray spectroscopy is used to determine the elemental compositions of NFs (EDS or EDXA). EDS is a kind of analytical measuring instrument that is mostly used to characterize the chemical compositions of various materials [17]. Every element in the periodic table has a particular electronic structure, and when the material is blasted with accelerated incident electrons, each element's reaction to assaulted electromagnetic waves, such as output characteristic X-rays of a certain wavelength, is unique. Chemical analysis may be done using the information from these output characteristic X-rays. EDS[4] may also be used to determine the amount of particle surface coating materials and the degree of oxidation of NFs [18].

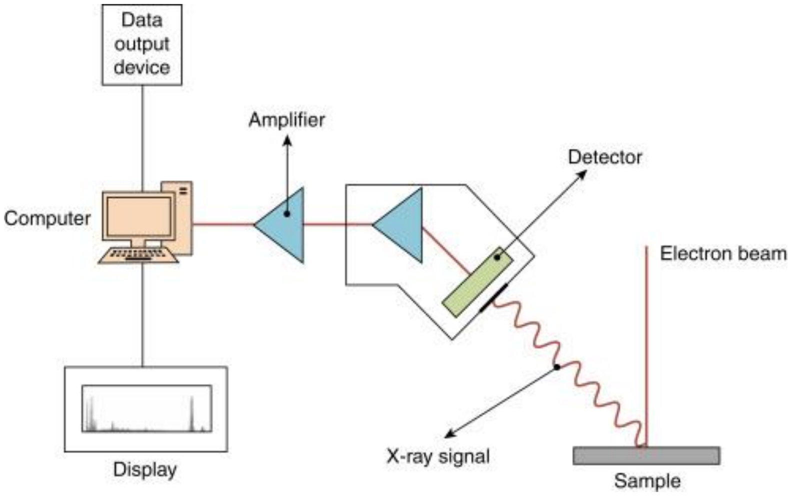

Figure 3-13: schematic of Energy-dispersive X-ray spectroscopy [37].

3.3.2.1 Different modes of EDX

1) **Primary:** In this mode of operation, the SEM works with secondary electron imaging and a high-resolution power of roughly (1-5) nm [19-20]**.**

2) **Secondary:** It is associated with distinctive X-rays in secondary mode, which are utilized to identify the elemental composition of material samples using the EDX method [19-20].

3) **Tertiary:** In tertiary mode, electronic pictures are backscattered. It also tracks the test sample's elemental makeup [19-20].

3.3.3 UV-Vis Spectroscopy

UV spectroscopy is the study of absorption and reflectance spectroscopy in the ultraviolet and visible electromagnetic spectrum. The absorption happens due to the electronic transitions from the ground state to the excited state and its magnitude depends on the Beer-Lambert law. Absorption occurs as a result of electronic transitions from the ground to excited states, and its magnitude is determined by the Beer-Lambert equation [21]. The UV-VIS Spectrometer's working principle is based on

1) Absorption spectroscopy
2) Emission spectroscopy

Absorption spectroscopy is an analytical method for determining the absorption of electromagnetic (EM) radiations. Ultraviolet, visible, and infrared radiations have wavelength ranges of 10-400 nm, 400-800 nm, and 0.76-15 m, respectively, and absorption spectroscopy is used to quantify EM radiation in these wavelength ranges. It spans from 200 nm to 400 nm in the near UV area, and below 200 nm in the far UV range; far UV spectroscopy is investigated in vacuum [22].

In another measuring approach (emission spectroscopy), a particle's or radiation's emission is distributed according to its properties, and the quantity of distribution is measured. Mass spectrometry is one example of this technology [22].

3.3.3.1 Working Principle of UV-Vis Spectroscopy

The basic schematic model shown in figure 3.17 covers most modern UV-Vis Spectrometers. It is made up of two lamps (one for UV light and the other for Vis light), as well as mirrors, prisms, and the necessary detector. The light's wavelength is successfully changed by a spectrometer and directed through a sample from higher wavelength (low energy) to lower wavelength (high energy). When the sample is exposed to the UV-Vis spectrum, electrons are excited to higher antibonding orbitals due to longer wavelength radiations [23]. On the X-axis, the graph between light absorption or transmittance and various wavelengths on the Y-axis is generated and examined. Absorbance (A) can be calculated as follows

$$\boldsymbol{A = log\left(\frac{1}{T}\right)} \tag{3.1}$$

Whereas A= Absorbance

And T = Transmittance

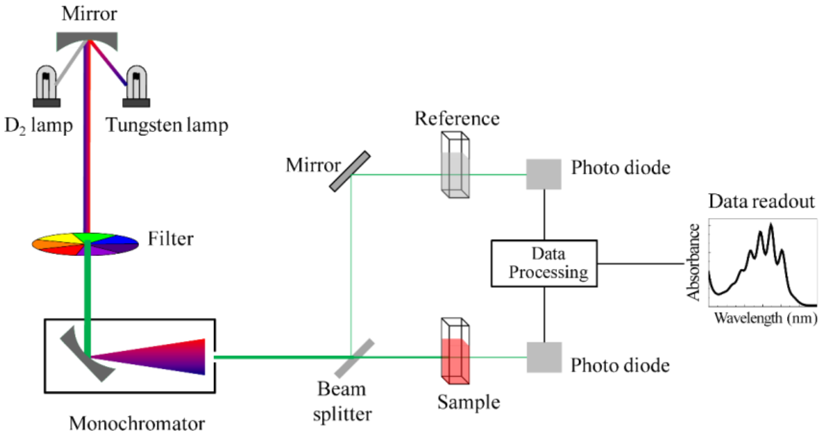

Figure 3-14: Schematic of UV-Visible Spectrometer.

3.3.4 Fourier transform infrared radiation spectroscopy (FTIR)

Infrared spectroscopy employing a Fourier Transform Infrared Radiation (FTIR) spectrometer is known as Fourier Transform Infrared Radiation (FTIR). It's a common characterization method used mostly in organic and polymer chemistry. It uses the unique absorption of infrared light to identify molecules and compounds. Because numerous organic and inorganic compounds are found in this part of the infrared spectrum, the wavelength range of 400 cm^{-1}-4000 cm^{-1} is employed [24].

3.3.4.1 **Working Principle of FTIR**

When infrared radiation (IR) strikes a sample, it absorbs certain wavelengths of the IR spectrum while allowing the rest to flow through. The activation of the vibrational energy levels occurs as a result of the absorption of radiation, resulting in a vibrational energy gap. The frequency of the absorption peak determines the vibrational energy gap; hence a certain frequency will have a specific vibrational energy gap. Similarly, the number of absorption peaks determines a molecule's vibrational freedom, and the strength of the absorption peak determines the molecule's dipole movement. The absorption, intensity, frequency, and number of absorption peaks are all distinct for each molecule and have particular values for each molecule, giving these molecules a fingerprint-like individuality. When a sample is analyzed using an FTIR spectrometer, the absorption, intensity, frequency, and number of absorption peaks are compared to the data directory already on hand, revealing the unknown chemical [25-26]. The FTIR spectrometer setup is shown in figure 3.18.

Figure 3-15 : FTIR spectrometer Cary 630 [38].

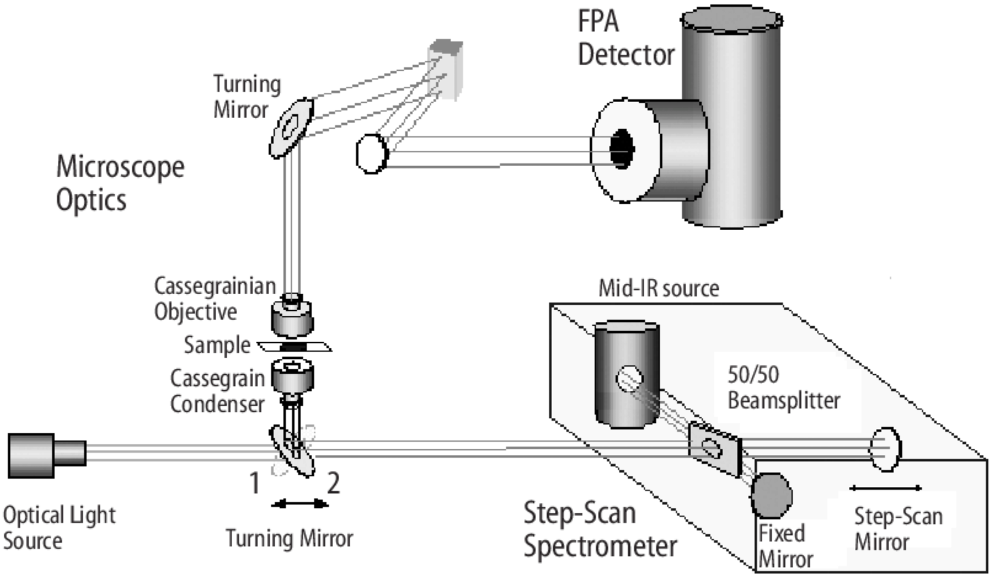

Figure 3-16: Schematic Diagram of a Fourier transform infrared radiation spectroscopy (FTIR) Imaging Spectrometer.

3.3.4.2 Molecular and compound identification (Functional Group Analysis)

A compound is a mixture of two or more elements. When an FTIR spectrometer is used to analyze a sample of an unknown organic or inorganic chemical or polymer. A unique spectrum of transmittance at the y-axis versus the wavelength at the x-axis is produced. A spectrum has several peaks, each of which corresponds to a distinct chemical or bond [27]. The value of wavelength for each acquired peak is compared to the FTIR data directory, which lists bonds or molecules that correspond to distinct wavelengths. We can learn about the bond or molecule present in the sample by matching those wavelengths with molecules, and we can locate the unknown substance by understanding these molecules and bonds [28].

3.3.5 Hall Effect Measurement

The Van der Pauw technique is widely used to measure resistivity, sheet resistance, mobility, and material type. The approach needs thin sheets of homogenous, symmetrical materials. The contacts must also be evenly spaced, throughout the periphery, and smaller than the film area. If the preceding requirements are met, then

$$\boldsymbol{e^{-(\pi\frac{d+R_{AB,CD}}{\mathcal{P}})} + e^{-\left(\pi\frac{d+R_{BC,AD}}{\mathcal{P}}\right)} = 1} \tag{3.2}$$

A and B are resistances when electricity is applied. Potentiometers measure the potential between C and D. Resistance is estimated for current entering from B and exiting from C, when potential is measured between A and D. The letter ‘d' represents sample thickness, while ‘p' represents resistivity.

Figure 3-17: HMS 300 hall effect measurement system [39].

3.3.6 IV Characteristic Measurement

For the characterization of the photovoltaic performance of solar cells solar simulators are used. A class AAA solar simulator Newport Oriel IV station with Keithley PVIV 2400 source meter was used for IV measurement. Major parts of the solar simulator include a light source for the production of artificial light, a power supply to power the lamp, and optics to concertation the light toward the work surface. Figure 3.21 shows the simple working of the solar simulator [33].

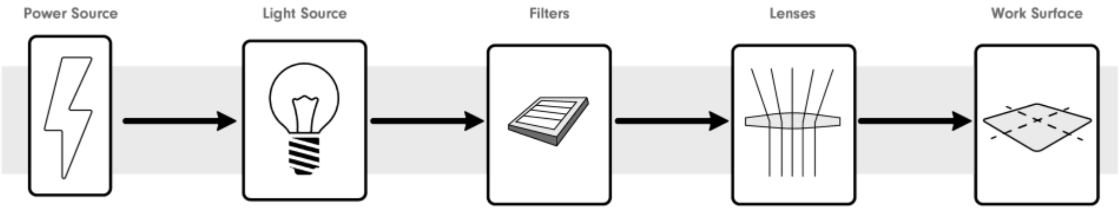

Figure 3-18: A simple setup of the solar simulator [29].

A Solar simulator should have the following have requirements for optimum measurements of photovoltaic devices [29-30]:

1) Spectrum: Spectral Energy maximum allowable deviation. To measure spectral irradiance spectroradiometers [31] are used and sometimes specially filtered Photovoltaic cells [32].
2) Uniformity of the irradiance
3) Stability of the beam light

3.3.6.1 **Working Principle of Solar simulator**

Solar simulators are used to produce a light spectrum approximating a standard solar spectrum and irradiance (or intensity). A solar simulator may be of class A, B, or C category per ASTM. A spectral mismatch for the test cell, reference device, and standard spectrum (of interest) may be useful in evaluating the classifying a simulator. Before J–V measurements, the simulated light is set to match the standard spectrum and intensity by employing a reference cell for the specific device. Other than the spectrum and irradiance, the effective area of a cell must be specified for J–V measurements, because the output current density is dependent not only on the output current but also on the effective cell area (active area) [33].

Figure 3-19 **:** Newport Oriel IV station [40].

The type of parameters that are measured by the solar simulator are [33]

1) **Short Circuit Current (I_{SC})**: When the circuit of the solar cell is shorted I_{SC} is delivered with a voltage equal to zero. On the curve, it is the point when Voltage is zero.

2) **Open Circuit Voltage (V_{OC}):** When the current is zero V_{OC} is obtained. On the curve, it's the point when the current is zero.

3) **Maximum Power Point (MPP):** MPP is an operating point at which maximum power is obtained. Corresponding voltage and current points are called V_{MPP} and I_{MPP} respectively.

4) **Fill Factor (FF):** Fill Factor is the ratio of MPP and product of V_{OC} and I_{SC}. On the curve, it's the area under MPP compared to the area of V_{OC} and I_{SC}

5) **Efficiency (η %):** The efficiency of the solar cell is defined as the ratio of obtained electrical power to incident optical power.

Summary

In this chapter different wet chemistry routes for the synthesis of photoanode of DSSC were discussed then afterward different routes for the synthesis of nanofibers were discussed. We used electrospinning for the synthesis of Nanofibers on FTO. LE-10 by Bionica was used for different depositions. To evaluate and study the deposition different characterization techniques were used. Firstly, a Scanning electron microscope (SEM) and EDX were used to analyze the morphology and chemical composition of the Nanofibers. Secondly, FTIR was used to observe the functional group and structural analysis of the electro-spun NFs. Then, Hall Effect and UV-Vis Spectrophotometer were employed to determine the electrical and optical properties of the nanofibers. Finally, a solar simulator was used to study the IV characteristic of the solar cell, respectively. In a nutshell, an efficient methodology was finalized for the synthesis of DSSC's photoanode.

References

[1]. X. Chen and S. S. Mao, Chem. Rev., 2007, 107(7), 2891–2959.

[2]. Beachley V, Wen X (2020) Polymer nanofibrous structures: fabrication, biofunctionalization and cell interactions. Prog Polym Sci J 35(7):868–892. https://doi.org/10.1016/j. progpolymsci.2010.03.003.

[3]. Zheng-Ming H, Zhang Y-Z, Kotaki M, Ramakrishna S (2003) A review on polymer nanofibers by electrospinning and their applications in nanocomposites. Compos Sci Technol 63:2223–2253.

[4]. Wang J, Nain AS (2019) Suspended micro/nanofiber hierarchical biological scaffolds fabricated using non-electrospinning STEP technique. Langmuir 30(45):13641–13649. https://doi.org/10.1021/la503011u.

[5]. Stojanovska E, Canbay E, Pampal ES, Calisir MD, Agma O, Polat Y, Simsek R, Serhat Gundogdu NA, Akgul Y, Kilic A (2016) A review on non-electro nanofibre spinning techniques. RSC Adv 87:83783–83801.

[6]. Zhang X, Lua Y (2019) Centrifugal spinning: an alternative approach to fabricate nanofibers at high speed and low cost. Polym Rev 54:677–701.

[7]. Kumar P (2012) Effect of collector on electrospinning to fabricate aligned nanofiber. Department of Biotechnology & Medical Engineering National Institute of Technology, Rourkela.

[8]. Reneker, D. H.; Yarin, A. L. ‘Electrospinning jets and polymer nanofibers.’ Polymer 49 (2008): 2387–2425; (b) Luo, C. J.; Stoyanov, S. D.; Stride, E.; Pelan, E.; Edirisinghe, M. ‘Electrospinning versus fibre production methods: from specifics to technological convergence.’ Chem. Soc. Rev. 41 (2021): 4708–4735.

[9]. Cooley, J. F. Improved methods of and apparatus for electrically separating the relatively volatile liquid component from the component of relatively fixed substances of composite fluids. Patent number GB 06385, 1900.

[10]. Zeleny, J. ‘Instability of electrified liquid surfaces.’ Phys. Rev. 10 (1917): 1–6; (b) Zeleny, J. ‘The electrical discharge from liquid points, and a hydrostatic method of measuring the electric intensity at their surfaces.’ Phys. Rev. 7 (1914): 69–91.

[11]. Formhals, A. Process and apparatus for preparing artificial threads. Patent number US 1975504, 1934.

[12]. Formhals, A. Method and apparatus for spinning. Patent number US 2160962, 1939.

[13]. Sampath Kumar, T.S., 2013. Physical and chemical characterization of biomaterials A2. In: Bandyopadhyay, A., Bose, S. (Eds.), Characterization of Biomaterials. AcademicPress, Oxford, Chapter 2.

[14]. Goldstein, J., 2021. Practical Scanning Electron Microscopy: Electron and Ion Microprobe Analysis. Springer Science & Business Media.

[15]. Pathak, Y., Thassu, D., 2016. Drug Delivery Nanoparticles Formulation and Characterization. CRC Press.

[16]. Takahashi, C., Ogawa, N., Kawashima, Y., Yamamoto, H., 2015. Observation of antibacterial effect of biodegradable polymeric nanoparticles on Staphylococcus epidermidis biofilm using FE-SEM with an ionic liquid.

[17]. Hodoroaba, V.-D., Motzkus, C., Mace´, T., Vaslin-Reimann, S., 2019a. Performance of high-resolution SEM/EDX systems equipped with transmission mode (TSEM) for imaging and measurement of size and size distribution.

[18]. Kim, K., Unger, W., Kim, J., Moon, D., Gross, T., Hodoroaba, V.D., et al., 2021. Inter-laboratory comparison: quantitative surface analysis of thin Fe-Ni alloy films. Surface Interface Anal. 44 (2), 192199.

[19]. Hodoroaba, V.D., Rades, S., Unger, W.E., 2019b. Inspection of morphology and elemental imaging of single nanoparticles by high-resolution SEM/EDX in transmission mode. Surface Interface Anal. 46 (10-11), 945-948.

[20]. Thomas, S., Thomas, R., Zachariah, A.K., Mishra, R.K., 2017. Microscopy Methods in Nanomaterials Characterization. Elsevier.

[21]. Ikemura, K., Ichizawa, K., Yoshida, M., Ito, S., Endo, T., 2018. UV-VIS spectra and photoinitiation behaviors of acylphosphine oxide and bisacylphosphine oxide derivatives in unfilled, light-cured dental resins. Dent. Mater. J. 27, 765774.

[22]. F. Lanza, B. Sellergren, Anal. Chem. 71 (1999) 2092.

[23]. M.C. Burleigh, S. Dai, E.W. Hagaman, J.S. Lin, Chem. Mater. 13 (2001) 253.

[24]. Yu, P., Jonker, A., Gruber, M., 2009. Molecular basis of protein structure in proanthocyanidin and anthocyanin-enhanced Lc-transgenic alfalfa in relation to nutritive value using synchrotron-radiation FTIR microspectroscopy: a novel approach. Spectrochim. Acta A: Mol. Biomol. Spectrosc. 73, 846-853.

[25]. Harnly JM, Fields RE (1997) Appl Spectrosc 51:334A.

[26]. Snively CM, Katzenberger S, Oskarsdottir G, Lauterbach J (1999) 24:1841.

[27]. Arvanitopoulos C, Koenig JL (1996) Appl Spectrosc 50:11.

[28]. Noobut W, Koenig JL (1999) Polym Composite 20:38.

[29]. ISO/DIS15387:Space Systems Single-Junction Space Solar Cells Measurement and Calibration Procedures.

[30]. ESAPSS-01–604, Generic specification for silicon solar cells (1988).

[31]. C.H. Seaman, et al., The spectral irradiance of some solar simulators and its effect on cell measurements, in: Proceeding of the 14th IEEE Photovoltaic Specialists Conference, 1980, pp. 494–499. San Diego.

[32]. G.S. Goodelle, et al., Simulator spectral characterization using balloon calibrated solar cells with narrow band pass filters, in: Proceeding of the 15th IEEE Photovoltaic Specialists Conference, 1981, pp. 211–217. Orlando.

[33]. O. Kawasaki, et al., Study of solar simulator method and round robin calibration plan of primary standard solar cell for space use, in: Proceeding of the 1st World Conference on Photovoltaic Energy Conversion, 1994. Hawaii.

[34]. Fluidnatek-LE-10-web. (n.d.). Retrieved January 20, 2022, from https://bioinicia.com/electrospinning-electrospraying-lab-equipment/bioinicia-fluidnatek-le-10-web/

[35]. Abboodi, H. H., & Al-Dabagh, D. J. N. (2018). Analysis of two Different Types of Orthodontic Mini-Implants Immersed in Fluoridated Mouthwashes Using Scanning Electron Microscopy (SEM). International Journal of Medical Research & Health Sciences, 7(6), 23-31.

[36]. Administrator. (2019, June 14). Looking at materials up close - the scanning electron microscope. Retrieved January 20, 2022, from

https://www.rrutc.msm.cam.ac.uk/outreach/articles/the-scanning-electron-microscope

[37]. Colpan, C. O., Nalbant, Y., & Ercelik, M. (2018). 4.28 Fundamentals of Fuel Cell Technologies.

[38]. Cary 630 FTIR Spectrometer from https://www.agilent.com/en/product/molecular-spectroscopy.

[39]. Ecopia HMS-3000 Hall Measurement System from our-point-probes.com/ecopia-hms-3000-hall-measurement-system/

[40]. MPVIV-IV-Station from https://www.newport.com/medias/sys_master/software/software/h32/he9/9132470796318/MPVIV-IV-Station.pdf

Chapter 4 Experimental

4.1 Sample Preparation

4.1.1 Dimensions of the Sample

One of the components of DSSC is the substrate. There are different substrates used for the synthesis of DSSC. FTO and TCO are most commonly used. FTO coated glass was selected as a substrate and was purchased. The sheet resistance was 10 ohm/cm^2. The thickness of the sheet was 2mm. The bigger piece of the sheet was cut into smaller pieces with a 2x2 cm^2 dimension.

4.1.2 Cleaning of the sample

Cleaning of the substrate was done to remove and clean any type of debris present on the surface and substrate. A solution of distilled water, ethanol, and soap was prepared in a beaker. The FTOs were placed inside the beaker. This beaker was placed inside a sonicator for sonication. The temperature was kept at 100℃ and the time of sonication was 1 hour.

4.2 Synthesis of the Solution

4.2.1 Materials.

Materials for experimentation are Titanium (IV) isopropoxide (TTIP), 95 % ($C_{12}H_{28}O_4Ti$) was purchased from Alfa Aesar. Polyvinyl pyrrolidone (PVP) ((C_6H_9NO)n), MW= 90,000 gmol^{-1} was purchased from Sigma-Aldrich. Copper (II) Chloride Dihydrate ($CuCl_2.2H_20$) was purchased from Innovating Science. Ethanol absolute (C_2H_5OH) was purchased from VWR International. Acetic acid was purchased from sigma Sigma-Aldrich. Fluorine Doped Tin Oxide (FTO) coated glass was purchased from Nanoshel. N3 dye was purchased from Sigma-Aldrich. The platinum paste was purchased from Sigma-Aldrich. used as raw materials in this study.

4.2.2 Doping Percentage

In order to calculate the doping percentage of dopant percentage, the weight of the $CuCl_2.2H_20$ was measured because the dopant percentage is controlled by the weight of dopant relative to volume density of TTIP. The relationship between mass and volume is

$$\boldsymbol{m = \frac{\rho}{V}} \qquad \textbf{(4.1)}$$

were,

ρ =density of the liquid in g/cm^3

m = mass of in grams (dopant)

and V = volume in cm^3

4.2.3 Solution Preparation

2ml of Titanium (IV) isopropoxide (TTIP) was mixed in a 15ml solution of ethanol and acetic acidic (4:1) and stirred for 30 mins at 800 rpm at ambient temperature. 0.07g Copper (II) Chloride Dihydrate $CuCl_2.2H2O$ was added to this solution. This solution was stirred for 2 hours. Then 0.2 g of PVP was dissolved into the solution and stirred for 30 mins.

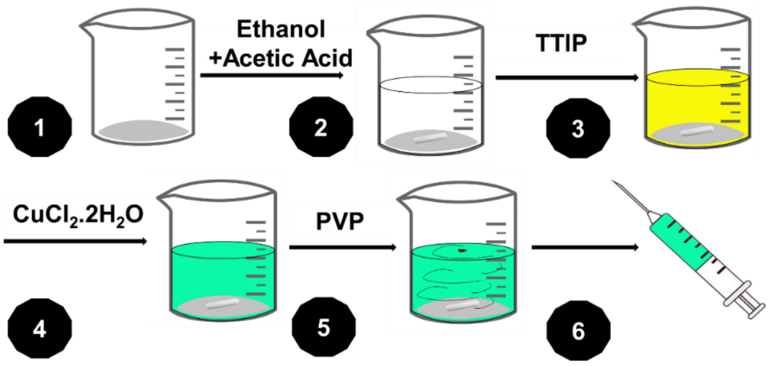

Figure 4-1: Steps for preparing the electrospinning solution

4.3 Electrospinning Experiments

For the synthesis of NFs FLUIDNATEK LE-10 by Bioinicia was used.

4.3.1 Preparation of Sample

For the placement of the substrate, a stationary collector was used. Upon stationery collector, aluminum foil was warped. FTO glass that was cut into 2 cm x 2 cm pieces and cleaned is placed onto the aluminum foil. The prepared FTOs were place inside beaker with a solution of distilled water, ethanol, and soap. The temperature was kept at 100℃ and the time of sonication was 30 min. The cleaned FTOs were attached to the front side of the collector with the help of conductive carbon tape. The prepared solution was loaded into a syringe and was fitted inside the pumps of the machine.

4.3.2 Preparation of Mask

In order to get a photoanode of a specific size and shape, a mask was prepared to cover the front side of the FTO. A punch hole was used to cut the area.

4.3.3 Parameters for Electrospinning

14 kV was applied, the feed rate was kept at 0.7 ml/hr and needle to collector distance was kept between 10 cm and 20 cm for different prepared solutions. The solution was electrospun for not more than 30 mins.

Table 4-1 Deposition Parameter for fabricated NFs via Electrospinning Technique.

Precursor Sol.	**Substrate**	**Needle Tip to Collector distance (cm)**	**Voltage (kV)**	**Flow rate (µL/hr)**	**Deposition time (mins)**
$CuCl_2.2H_2O$ TTIP Ethanol Acetic Acid PVP	FTO slide Aluminum foil	10	14	1000	15

4.4 Synthesis of Cu doped TiO_2 Nanofibers (NFs)Photoanode

The NFs were deposited on the conductive side of FTO glass. FTO glass was detached from the collectors and dried for 1 hr in a drying oven at 100℃. Then Heat treatment was done to get the photoanode. The sample was carefully placed inside a silica boat and was wrapped inside an aluminum foil. This dried sample was annealed in a thermal furnace at 500℃ for 2h and the heating rate was kept at 2℃/min. Hence photoanode was prepared [3].

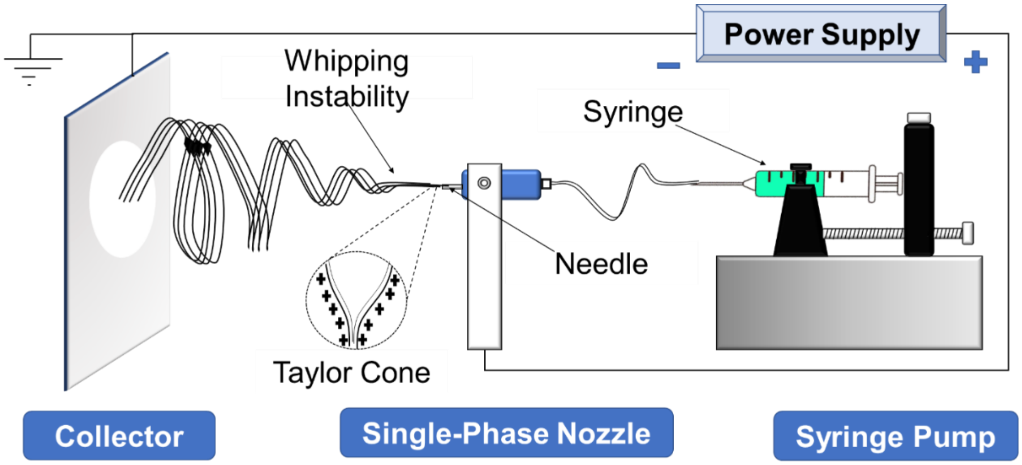

Figure 4-2: Electrospinning Setup with power supply, collector, nozzle, and syringe pump.

4.5 Experiments for Cu doped TiO_2 NFs

There was a variety of experiments performed to achieve the Cu-TiO_2 NFs. Different concentration of PVP was mixed in solution to get different morphology.

Table 4-2 Variable quantity of dopant

Experiments	Precursors	Parameters
01	01. TTIP = 2 ml	Voltage =10 kV
	02. PVP = 0.4 g	Flow Rate =1000 uL/h
	03. Ethanol = 12 ml	Distance =10 cm

	04. Acetic Acid = 3ml	
	05. $CuCl_2.2H_2O$ = 0.035 g	
02	01. TTIP = 2 ml	Voltage =10 kV
	02. PVP = 0.4 g	Flow Rate =1000 uL/h
	03. Ethanol= 12 ml	Distance =10 cm
	04. Acetic Acid =3ml	

4.6 Fabrication of Device

4.6.1 Synthesis of the Electrolyte

For the synthesis of Electrolyte guanidinium thiocyanate (0.10 M), 4-tert-butylpyridine (0.50 M), iodine (0.03 M) and iodide (0.60 M) were mixed in a solution of acetonitrile and valeronitrile (85: 15). This solution was stirred for 30 min to get the desired solution of Electrolyte.

4.6.2 Dye Sensitization

0.3 mM of N3 dye solution in ethanol was used. The prepared photoanode was kept in the dye for 24 hours.

Microfluidic solar cells were created to provide control, reliability, and repeatability in a simple system. It contains a PMMA clamping system, a PDMS interconnection, FTO, a PDMS layer, and thin copper foil. The photoanode was placed below. A layer of copper foil and PDMS membrane was placed. Upon these layers FTO coated with Pt was placed. This prepared setup was sandwiched between the clamping system and tightened with screws. Then electrolyte was inserted with the help of a dropper and sealed with sealant. Furthermore, reversibility of the sealing is intended to enable post-use examination of the prototypes [1]. Figure 4.3 shows an exploded schematic of a microfluidic DSSC and an image of the finished device [2].

4.6.3 Microfluidic Structure

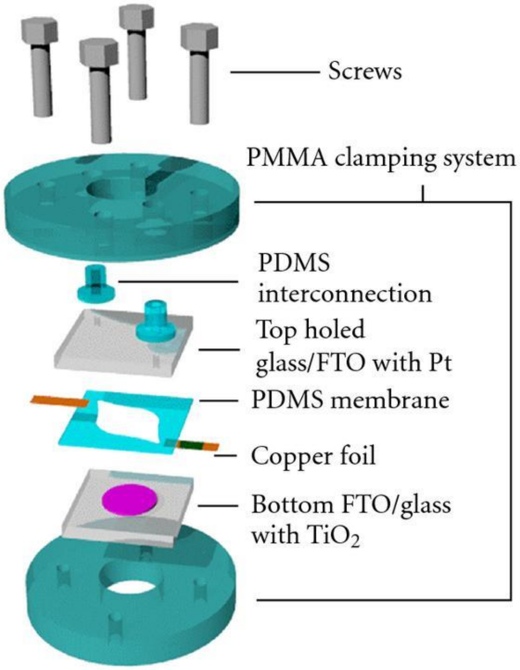

Figure 4-3: A Microfluidic structure assembly [2].

4.7 Testing and Characterizations

Morphological, crystalline, and Electrooptical properties of the prepared photoanode were studied using different characterization techniques.

1) SEM was used to analyze the morphology of the fibers.
2) EDX was employed to check the elemental composition of the fibers.
3) UV-Vis was used to know the optical properties of the photoanode.
4) Hall effect was employed to check the conductivities of electrospun NFs and annealed samples. The electrical performance of the device was measured using the system.
5) FTIR Spectroscopy was used to study the functional groups.
6) Solar Simulator was used for photovoltaic characterization. V_{OC}, J_{SC}, FF, and efficiency were measured.

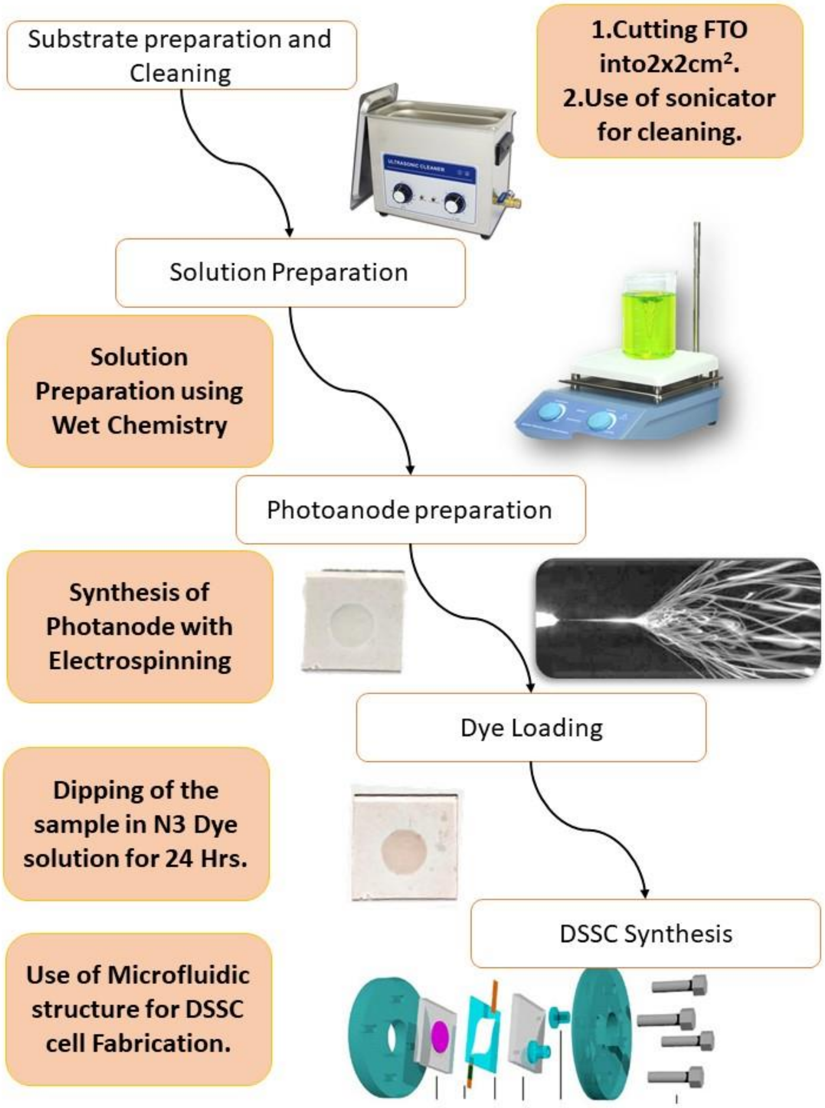

Figure 4-4: Schematic Diagram for the steps involved in Fabrication of DSSC

Summary

In this chapter methodology for the synthesis of Cu doped TiO_2 NFs was discussed. The Electrospinning technique was used for the fabrication of the photoanode of DSSC. For the preparation of Electrospinning solution, TTIP which is the source of TiO_2 was mixed in solution Ethanol and Acetic Acid. To this solution, PVP (polymer) was added. For Cu doping, $CuCl_2.2H_2O$ was used. Different concentration of $CuCl_2.2H_2O$ was added to the solution for different doping concentrations. Then, the solution was loaded in pumps. The parameters Voltage= 10kV and Flow rate =1000 µL/hr were kept for electrospinning. The prepared photoanode was annealed at 500 ℃ for 2 hrs. at (2℃/min). This photoanode was dipped in N3 dye solution for 24 hrs. The photoanode color changed. This photoanode was placed inside a microfluidic structure for the fabrication of solar cells. Finally, the IV performance of solar was measured.

References

[1]. Ito, S., Murakami, T. N., Comte, P., Liska, P., Grätzel, C., Nazeeruddin, M. K., & Grätzel, M. (2008). Fabrication of thin film dye sensitized solar cells with solar to electric power conversion efficiency over 10%. Thin solid films, 516(14), 4613-4619.

[2]. Sacco, A., Lamberti, A., Quaglio, M., Bianco, S., Tresso, E., Alexe-Ionescu, A. L., & Pirri, C. F. (2012). Electric characterization and modeling of microfluidic-based dye-sensitized solar cell. International Journal of Photoenergy, 2012.

[3]. Zheng, X., Shen, Z. P., Cheng, C., Shi, L., Cheng, R., & Dong, J. (2017). Electrospinning Cu–TiO 2 nanofibers used for photocatalytic disinfection of bacteriophage f2: preparation, optimization and characterization. RSC advances, 7(82), 52172-52179.

Chapter 5 Results and Discussion

5.1 Morphological analysis of Cu-TiO_2 NFs

Figure 5.2 shows the 3% Cu doped TiO_2 NFs before and after calcination. The surface morphology of nanofibers calcined at 500°C was observed. These images reveal the conversion of PVP NFs into Cu-TiO_2 NFs after calcination. The calcined samples showed successful development of Cu-$TiO_{2,}$ and it was confirmed with EDX and FTIR. Histogram and gaussian distribution function were applied to evaluate the average diameter of the nanofibers. The average diameter of the non-annealed nanofibers was 170.2 nm while for the annealed nanofibers was 95.7 nm. The efficiency of the solar cell is directly related to the diameter of the nanofibers. The mean diameter decreased after the calcination which indicates the evaporation of PVP, and solvents, and that was confirmed from EDX and FTIR. As shown in table 3. The data shows that before calcination there was confirmation of several elements due to the presence of PVP, titania, copper, and other solvents. After the calcination, PVP and other solvents were evaporated except titania and copper. EDX spectra confirm that after calcination we have pure copper doped titania NFs.

The post calcined samples were rougher and have porous structures due to the evaporation of PVP and organic contents. Mesoporous structures were found in the annealed NFs. These structures not only provide suitable energy levels for efficient charge transportation from dye molecules but also continuous structures for better charge mobility [8]. Continuous structure of NFs was observed for calcined samples. These continuous structures are very helpful in charge transport and provide high charge mobility due to less discontinuity of the path [9]. Thus, these structures can improve the current density and power conversion efficiency of the solar cell.

Table 5-1 Atomic %age of different elements in bare TiO_2 NFs and Cu-Doped TiO_2 NFs.

Sample	Ti	O	Cu	C	Cl
Non-Calcined Nanofibers	3.74	75.16	0.06	20.70	0.03
Calcined Nanofibers	20.62	79.22	0.17	0	0

NOTE: Ti-Titanium, O-Oxygen, Cu-Copper, C-Carbon, Cl-Chlorine.

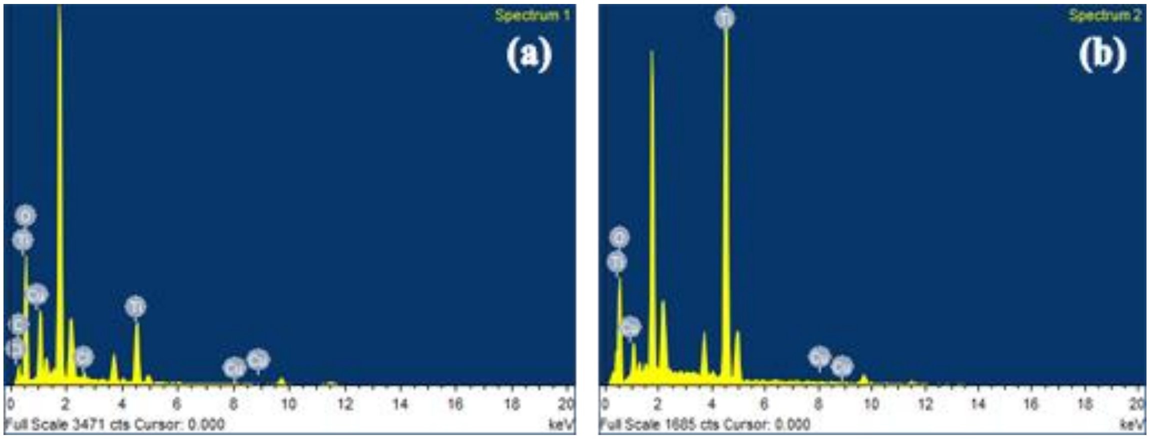

Figure 5-1: (a) EDX spectra for uncalcined sample (b) EDX data for calcined at 500^{o}C

5.2 Structural analysis of Cu-TiO_2 NFs

FTIR was used to analyze the functional group and structural analysis of the desired material. As shown in figure 5.3, FTIR results reveal that before calcination there was an intense peak of carbon, hydrogenated carbon, and O-H at 1283 cm^{-1}, 1426 cm^{-1}, 1539 cm^{-1}, 1630 cm$^{-1,}$ and 3178 cm^{-1}.due to the presence of PVP, solvents, water, and a hydroxyl group. The presence of anatase copper doped titania was in the range of 400 cm^{-1} to 800 cm^{-1}. These results are much correlated to the previous findings [10]. After calcination at 500^{o}C, there was no peak of carbon and C-H except anatase titania on the FTIR spectra because the evaporation point of PVP is below 400℃ to 450 ℃. The peak after calcination validates that there was no presence of water, hydroxyl, and hydrocarbon in NFs after the heating treatment. Only nanofibers of Cu-doped Titania were left behind after the calcination of the material.

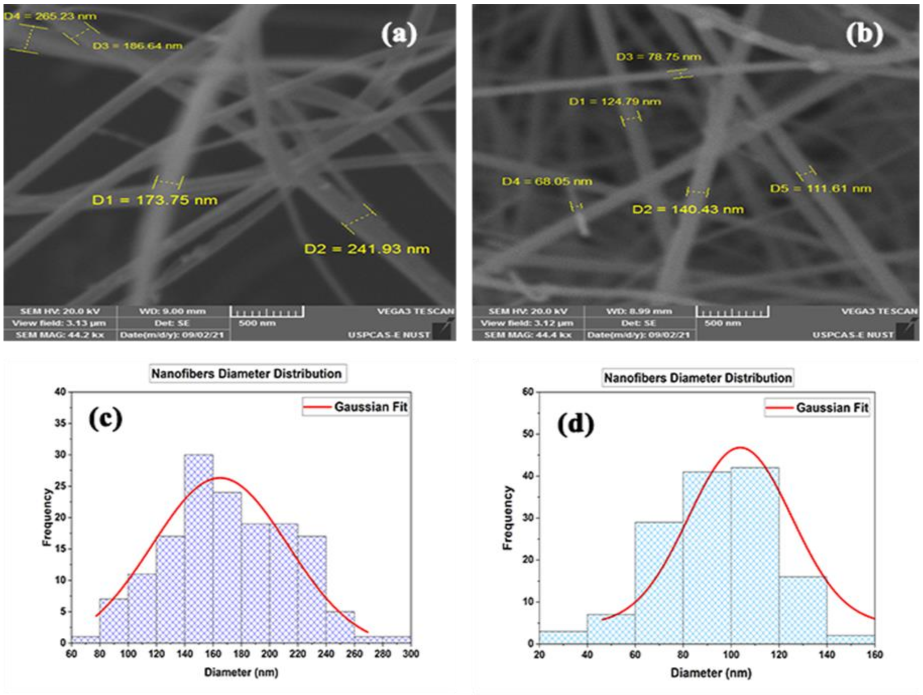

Figure 5-2: (a) 3% Cu doped TiO_2 before calcination (b) 3% Cu doped TiO_2 after calcination (c) Histogram and Gaussian fitting on uncalcined samples (d) Histogram and Gaussian fitting of a calcined sample at 500 C.

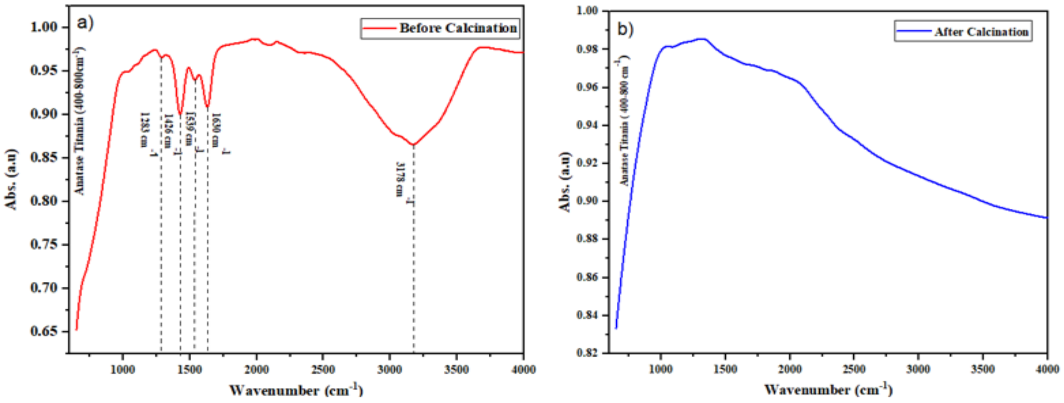

Figure 5-3: a) FTIR spectra before calcination b) FTIR spectra after calcination at 500°C

5.3 UV-Vis NIR analysis of Cu-TiO_2 NFs

To analyze the optical properties of photoanode UV-Vis was performed and is displayed in figure 5.4 and figure 5.5. Bare TiO_2 NFs have a bandgap of 3.7 eV and the maximum absorption of the spectrum was around 280 nm. The absorption peaks are obtained when an electron is excited to the conduction band (CB) from the Valence band (VB) [1]. However, there was negligible absorbance beyond 314nm which shows that the absorption in the visible region of the EM spectrum is nearly equal to zero. When Titania is doped with metals the material properties to Titania are altered mainly due to the presence of Cu^{2+} ion on the surface as well as inside bulk TiO_2 [3-5]. It can be seen that the bandgap TiO_2 has improved with Cu doping this reduces the V_{OC} but this caused an increase in electron injection efficiency [17].

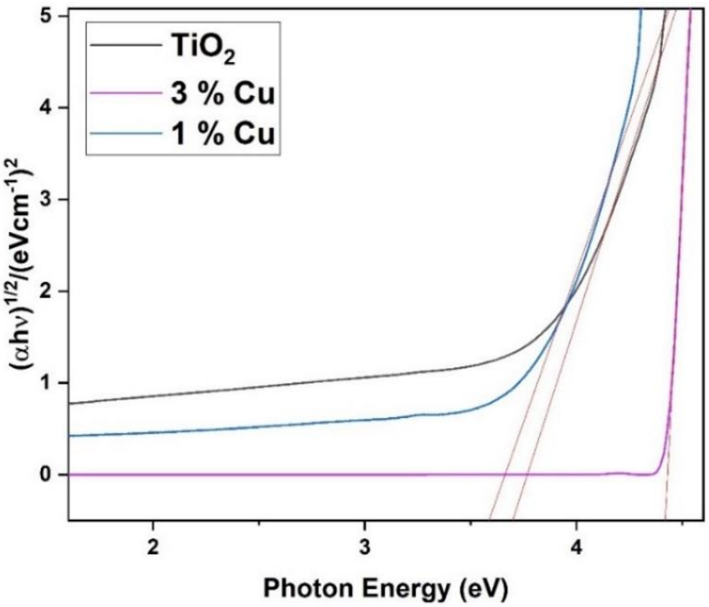

Figure 5-4: Tauc Plot for Absorption spectra of Titania and Cu doped Titania Nanofibers.

At 1% Cu, doped TiO_2 NFs have a bandgap of 3.5 eV, and absorption of the spectrum was from 200 nm to 340 nm. the maximum absorption of the spectrum was around 288 nm. Negligible absorbance was observed beyond 340 nm. At 3% Cu, doped TiO_2 NFs have a bandgap of 4.4 eV, and absorption of the spectrum was from 250 nm to 285 nm. Negligible absorbance was observed beyond 285nm. Most of the spectrum was absorbed in the ultraviolet (UV) region of the irradiation. The UV-vis of Cu-TiO_2 NFs shows the shift of absorbance towards the UV region [2]. Due to the substitution of Cu^{2+} in the lattice structure of TiO_2, defects are generated which causes a change in optical response.

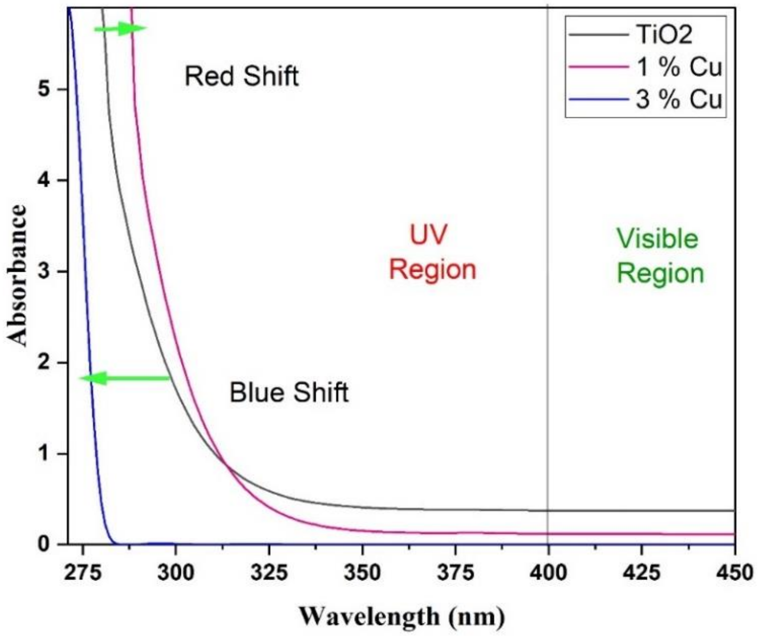

Figure 5-5: Absorption spectra of Titania and Cu doped Titania Nanofibers.

5.4 Hall Effect Measurements of Cu-TiO_2 NFs

Electrical properties of the bare TiO_2 NFs and Cu-TiO_2 NFs were analyzed by using the hall effect. Bulk concentration, Conductivity, Resistivity, and semiconductor type were determined by using this technique. For TiO_2 NFs, the carrier concentration was $3.2x10^{11}$, for 1% doped Cu-TiO_2 NFs it was $4.53x10^{+11}$, for 3% doped Cu-TiO_2 NFs it was 7.1 $x10^{11}$, the bulk concentration has increased by 2.2 times (3%). Due to doping of Cu^{2+} in the TiO_2 lattice structure free carriers are generated which increase overall bulk concentration. As the concentration of carriers increased, the conductivity of the copper doped titania also enhanced as shown in table 6 [11]. The conductivity of Cu-TiO_2 NFs was (2.6 to3.5)$x10^{-6}$ S/cm, which lie well within the range of semiconductors. It is 2 times more than pure TiO_2 NFs which is attributed due to the large presence of free carriers.

The Hall Coefficient of both the samples was negative, therefore they are n-type semiconductors [12].

Table 5-2 Hall Effect Measurements of simple TiO_2 NFs and Cu-Doped TiO_2 NFs

Sample	***n_H*** (cm^{-3})	***ρ*** (Ω.cm)	***Σ*** (1/Ω.cm)	***Type***
TiO_2 Nanofibers	$3.2x10^{+11}$	$6.5\ x10^{+05}$	$1.5x10^{-06}$	n-Type
1 % Cu doped TiO_2 NFs	$4.53x10^{+11}$	$3.8x10^{+05}$	$2.612x10^{-06}$	n-Type
3 % Cu doped TiO_2 NFs	$7.1x10^{+11}$	$2.9x10^{+05}$	$3.5x10^{-06}$	n-Type

NOTE: n_H- Bulk Concentration, ρ-Resistivity, σ-Conductivity.

5.5 IV and Performance Measurement of the prepared DSSC solar cell

IV measurements for the prepared DSSC solar cell were performed. As shown in figure 5.6 the V_{OC} measured was 0.66 V, the I_{SC} was 0.03002 mA, J_{SC} was 0.038 mA/cm^2, the P_{MP} was 0.0089 mW, the V_{MP} was0.46, the I_{MP} was 0.01950 mA, the Fill Factor was 44.8 %, and the efficiency of the solar cell was 0.0114 %. As measured bandgap with the help of UV-Vis was 3.5 eV. The doping of the TiO_2 with Cu has shifted the conduction band. The bandgap is wide which helps in an increase in voltage (V_{OC}) across the device. This leads to a decrease in electron lifetime (inversely proportional to V_{OC}) and ejection which in turn reduces the J_{SC} [13]. Due to copper, there is a negative shift in V_{FB} and this gives larger values of V_{OC} [14].

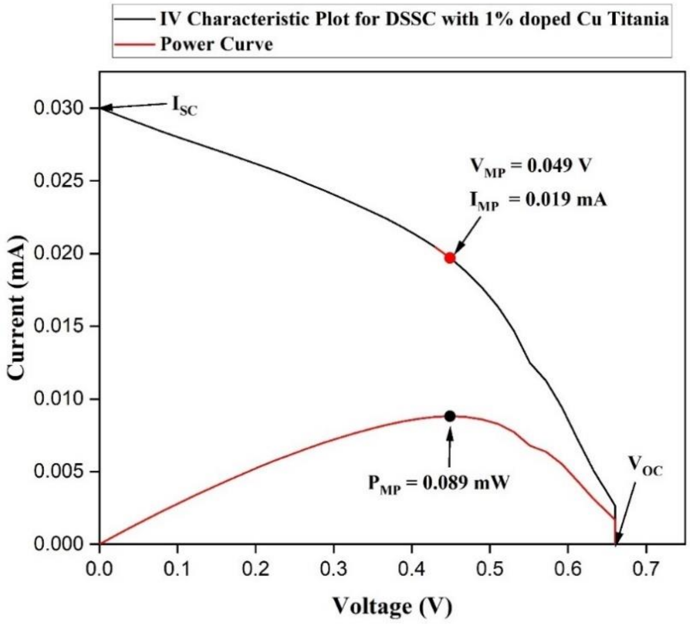

Figure 5-6: IV Characteristic of the Cu Doped Photoanode for DSSC

Table 5-3 Summary of the IV performance of Cu-doped TiO_2 NFs photoanode DSSC

Performance of DSSCs based on Cu-doped TiO_2 NFs photoanode					
Sample	**Jsc (mA cm^{-2})**	**Voc (V)**	**FF (%)**	**η (%)**	**P_{MP} (mW)**
1 % Cu doped TiO_2	0.038	0.66 V	44.8	0.0114	0.0089

Some studies also suggest that even if the dye adsorption is good, but the J_{SC} decreases due to Cu reaction with electrolyte and less electron ejection values [15]. The 1D structures have good charge transport but they have less surface area which may cause lower values of J_{SC} [16]. The fill factor defines the power that a photovoltaic device can deliver. By keeping shunt resistance higher and series resistance lower power delivery of device can be increased that can be done by matching the LUMO of dye with Conduction band of TiO_2. The Fill factor is defined by the rectangle under the (Maximum Power Point) MPP of the Curve.

References

[1]. Al-Attafi, K., et al., The effect of amorphous TiO 2 in P25 on dye-sensitized solar cell performance. 2018. 54(4): p. 381-384.

[2]. Unal, F.A., et al., Synthesis, characterization, and application of transition metals (Ni, Zr, and Fe) doped TiO2 photoelectrodes for dye-sensitized solar cells. 2020. 299: p. 112177.

[3]. Rajamanickam, N., K.J.J.o.C. Ramachandran, and I. Science, Improved photovoltaic performance in nano TiO2 based dye sensitized solar cells: Effect of TiCl4 treatment and Sr doping. 2020. 580: p. 407-418.

[4]. Nguyen, H.H., et al., Physicochemical properties of Cr-doped TiO2 nanotubes and their application in dye-sensitized solar cells. 2020. 397: p. 112514.

[5]. Sun, J., et al., Ag-decorated TiO2 nanofibers for highly efficient dye sensitized solar cell. 2020. 260: p. 126882.

[6]. Sista, D., New Perspective of Nano Fibers: Synthesis and Applications. 2021.

[7]. Barhoum, A., M. Bechelany, and A.S.H. Makhlouf, Handbook of nanofibers. 2019: Springer.

[8]. Mali, S.S., et al., Evaluation of various diameters of titanium oxide nanofibers for efficient dye sensitized solar cells synthesized by electrospinning technique: A systematic study and their application. 2015. 166: p. 356-366.

[9]. Hussein, A.M., et al., Interconnected ZrO2 doped ZnO/TiO2 network photoanode for dye-sensitized solar cells. 2018. 4: p. 56-64.

[10]. Ansari, Z., et al., Dye sensitized solar cells fabricated using Cu-Doped TiO2 nanopowder with anthocyanin as sensitizer. 2015. 10(2): p. 290-294.

[11]. Li, R., et al., Influence of charge carriers concentration and mobility on the gas sensing behavior of tin dioxide thin films. 2019. 9(9): p. 591.

[12]. Mazhir, S.N. and N.H.J.J.o.A.P. Harb, Influence of concentration on the structural, optical and electrical properties of TiO2: CuO thin film Fabricate by PLD. 2015. 7(6): p. 14-21.

[13]. C. Zhang, S. Chen, L. Mo, Y. Huang, H. Tian, L. Hu, Z. Huo, S. Dai, F. Kong and X. Pan, J. Phys. Chem. C, 2011, 115(33), 16418–16424.

[14]. B. Yacoubi, L. Samet, J. Bennaceur, A. Lamouchi and R. Chtourou, Mater. Sci. Semicond. Process., 2015, 30, 361–367.

[15]. J. Navas, C. Fernandez-Lorenzo, T. Aguilar, R. Alcantara and J. Martin-Calleja, Phys. Status Solidi A, 2012, 209(2), 378–385.

[16]. A. Lamberti, A. Sacco, S. Bianco, D. Manfredi, F. Cappelluti, S. Hernandez, M. Quaglio and C. F. Pirri, Phys. Chem. Chem. Phys., 2013, 15, 2596–2602.

[17]. M. R. Mohammadi, A. M. Bakhshayesh, F. Sadri and M. Masroor, J. Sol–Gel Sci. Technol., 2013, 67(1), 77–87.

Chapter 6 Conclusions and Recommendations

6.1 Conclusions

- Bare and Copper doped Titania NFs were successfully synthesized by using the electrospinning technique.
- SEM results reveal that size of the nanofibers was reduced and rougher after calcination at 500 ℃. EDS results confirm the presence of copper doping inside the titania.
- FTIR results elucidate that after calcination only copper doped titania was left behind and there was no peak of carbon, C-H, and a hydroxyl group.
- UV-Vis results show that bandgap decreased for 1% of copper in titania and increased after doping at 3% of copper in titania NFs. This is due to the substitution of Cu^{2+} in the lattice structure of TiO_2 the defects are generated which causes a change in optical response.
- Hall Effect results show that conductivity of the fibers increased by 2 times after doping of copper in titania NFs.
- These findings prove that Copper doped Titania has the potential to be utilized as a photoanode semiconductor material in the field of photovoltaics 3rd generation solar cells.

6.2 Future Recommendations

For commercial utilization of DSSCs, the efficiency needs to be increased. Following recommendations are suggested for more efficient and cost-effective DSSCs.

1. **Effective Doping**

   Doping is the better and effective way of modifying the electronic properties of TiO_2. For this purpose, metals (cationic doping) and nonmetals (anionic doping) are extensively used. Cationic and anionic dopings both can be done at once to take advantage. This means that doping that helps in better charge transport and dye adsorption can be used.

2. **Efficient use of Morphologies**

   Morphology is an important factor that directly affects the efficiency of semiconductors. For example, 1D structures like Nanotubes have better charge transport than nanoparticle structures but they have less surface area which means they adsorb less dye. By employing two different morphologies, we can drastically increase the efficiency of the solar cell.

3. **Optimization of Methods.**

   Each type of technique applied for the synthesis of DSSC has its pros and cons. Like posttreatment of the nanofibers in different solutions will increase the adhesion with the substrate. By complementing the different techniques with different will result in better and more efficient structures for DSSC.

4. **Use of Sensitizers**

   There are different dyes for the synthesis of DSSC. Some dyes are expensive like ruthenium-based dye. There needs to be research done on natural sensitizers to reduce the cost of dyes. These dyes are abundant and cheap. Their adsorption is one of the problems that need to be addressed.

5. Counter Electrode

Since Pt is the most commonly used catalyst for counter electrodes which is very expensive. Carbon-based catalysts are less costly and can easily be used. There need to be some work done on the effective synthesis process.

Appendix A

Electrospinning of Cu Doped TiO_2 Nanofibers and their potential application in Photoanode of Dye-Sensitized Solar Cells.

Wajahat Qasim[1, a], Zuhair Khan[1, b*], Aamir Satti[1, c], Asghar Ali[1, d], Altamash Shabbir[1, e], Zain Hussain[1, f]
[1]U.S.-Pakistan Centre for Advanced Studies in Energy (USPCAS-E),National University of Sciences and Technology (NUST), Sector H-12, Islamabad, Pakistan
[a]wqasimese19.ces@student.nust.edu.pk,
[b]zuhair@uspcase.nust.edu.pk,[c]aamirsatti@uspcase.nust.edu.pk,
[d]asghar@uspcase.nust.edu.pk,[e]mshabbirese19.ces@student.nust.edu.pk,
[f]zhussaintee19.ces@student.nust.edu.pk.

Keywords: Titania; Nanofibers; Cu-doping; Electrospinning.

Abstract

Titania (TiO_2) is an important material having found its use in many technological applications. Due to its large surface-to-volume ratio, TiO_2 nanofibers (NFs) are drawing increased attention in 3rd generation photovoltaic. The electro-optical response of TiO_2 can be tuned by metal doping and structural control at the nano level. In this research, NFs of copper (Cu) doped Titania (TiO_2) were fabricated by using electrospinning. To do away with Polyvinylpyrrolidone (PVP), the NFs were calcined and annealed in air at 500 ºC for 2 hours. The energy-dispersive X-ray spectroscopy (EDS) results confirmed the doping of copper inside the titania after calcination. Scanning electron microscopy (SEM) results show NFs of varying diameters mostly in the 80 nm to 200 nm regime. SEM of the post-annealed samples shows relatively rougher fibers of reduced size compared to the uncalcined samples. The increase in roughness and reduction in the NFs diameter means an increase in the overall surface area and more efficient charge transport as Hall's effect results depicted that after doping of copper in nanofibers, the conductivity improved by 2 times as compared to undoped nanofibers of titania. Moreover, Ultraviolet-visible Spectroscopy (UV-Vis) showed Cu doping shifted the absorption of the spectrum.

1.Introduction

With an increase in population, there is an increase in demand for electrical energy which is being met by different power generation methods. This huge energy demand can greatly affect the environment that can be tackled by using sustainable and green energy sources. Photovoltaics is one of the renewable energy sources that can help to reduce environmental problems. DSSCs are the 3rd generation of photovoltaics that is composed of a photoanode, electrolyte, and counter electrode. The performance of DSSCs majorly depends on these parameters.

There are several numbers of semiconductor materials that are utilized as a photoanode nowadays such as ZnO, SnO_2 and TiO_2, etc. Photoanode is composed of semiconductor material, Dye, and transparent conductive glass such as FTO and ITO. Morphological and structural response of semiconductor materials plays a vital role in the development of DSSCs. TiO_2 is widely used as a semiconductor material in DSSCs photoanode owing to its extensive properties and low cost [1]. However, the properties of TiO_2 are improved by increasing the conductivity of titania that helps to improve the efficiency of the DSSCs. This can be improved by employing various kinds of doping such as metal doping, nonmetal doping, doping of rare-earth metals, or their combinations [2]. Efficiencies for different kinds of metal and co-metal doping are summarized in table 1.

Table 0.1. Different kinds of doping in Titania and their respective efficiencies.

Reference	**Doping in TiO2**	**Voc**	**Jsc**	**Efficiency (%)**
Rajamanickam (2020) [3].	Sr doping in TiO2	0.78	18.53	9.6
Hao Huy Nguyen (2020) [4].	Cr-doped TiO2	0.69	18.75	7.5
Junmei Sun (2019) [5].	Ag- doped TiO2	0.812	11.24	6.36

Morphology of semiconductor material plays a crucial role in the performance of a solar cell. Incongruous morphology leads to poor charge collection and light scattering. Therefore, photoanode material with desirable morphology provides a good pathway for electron and light-harvesting that is utilized for the better performance of the cell. 1D nanostructure delivers a direct path for injected electrons as well as they can reduce recombinations. The surface area of the nanostructure is another hindrance in better dye loading and it greatly affects the overall efficiency of the solar cell. 1D Nanofibers can provide a better surface area for good dye loading. Employing these structures can lead to better charge transportation, light scattering, and surface area.

Nowadays, Nanofibers are manufactured by various techniques such as Electrospinning, Sonochemical synthesis, Polymerization, Template bases synthesis, and Self-Assembly, etc. Modern methods include Electro hydrodynamic, Plasma Induced synthesis, Centrifugal jet spinning, Electrohydrodynamic writing, CO_2 laser supersonics, and Plasma Induce synthesis [6]. Electrospinning is the most fascinating technique used for the synthesis of nanofibers. There are several numbers of ways to the utilization of electrospinning technique. Electrospinning is majorly dependent on deposition, type of solvent, needle, and the shape of the collector [7]. Single-phase nozzle and stationary collector are the most simple step-up for the synthesis of nanofibers using electrospinning.

In this present work, Titania and Cu doped TiO_2 NFs are fabricated through electrospinning. The morphological, structural, and optoelectrical behavior of NFs is investigated. In addition, the effect of copper doping in titania NFs have been also studied at various concentrations.

2.Experimental Setup

2.1 Materials and Method

Copper-doped Titania Nanofibers were fabricated through electrospinning technique (FLUIDNATEK LE-10 by Bioinicia). 2ml of Titanium (IV) isopropoxide (TTIP) was mixed in a 15ml solution of ethanol and acetic acidic (4:1) and stirred for 30 mins at 800 rpm at ambient temperature. 0.07g Copper (II) Chloride Dihydrate CuCl2.2H2O was added to this solution. This solution was stirred for 2 hours. Then 0.2 g of PVP was dissolved into the solution and stirred for 30 mins. A stationary collector was employed, upon which aluminum foil was warped. The prepared solution was loaded into a syringe and was placed inside the pumps of the machine. The voltage of 14 kV was applied; the feed rate was kept at 0.75 ml/hr and the needle to collector distance was 10 cm. The solution was electrospun for 15 mins. The NFs were deposited on the collector. The fibrous layer was detached from the collectors and dried for 1 hour in a drying oven at 100°C. After drying, the sample was placed in the muffle furnace for annealing at 500°C for 2 hours, and ramp was kept at 2℃/min.

Table 2: Deposition Parameter for fabricated NFs via Electrospinning Technique.

Precursor Sol.	***Substrate***	***Needle Tip to Collector distance (cm)***	***Voltage (kV)***	***Flow rate (µL/hr)***	***Deposition time (mins)***
• *$CuCl_2.2H_2O$* • *TTIP* • *Ethanol* • *Acetic Acid* • *PVP*	• *FTO slide* • *Aluminum foil*	*10*	*14*	*750*	*15*

3.Characterization

Scanning electron microscope (SEM) and EDX were used to analyze the morphology and elemental composition of the Nanofibers. FTIR was used to observe the functional group and structural analysis of the electro-spun NFs. Hall Effect and UV-Vis Spectrophotometer were employed to determine the electrical and optical properties of the nanofibers, respectively.

4.Results and Discussion

4.1 Morphology

Figures 2 a &b show the 3% Cu doped TiO_2 NFs before and after calcination. The surface morphology of nanofibers calcined at 500°C was observed. These images reveal the conversion of PVP NFs into Cu-TiO2 NFs after calcination. The calcined samples showed successful development of Cu-TiO_2, and it was confirmed with EDX and FTIR. Histogram and gaussian distribution function were applied to evaluate the average diameter of the nanofibers. The average diameter of the non-annealed nanofibers was 170.2 nm while for the annealed nanofibers was 95.7 nm. The efficiency of the solar cell is directly related to the diameter of the nanofibers. The mean diameter decreased after the calcination which indicates the evaporation of PVP, and solvents and that was confirmed from EDX and FTIR. As shown in table 3. The data shows that before calcination there was confirmation of several elements due to the presence of PVP, titania, copper, and other solvents. After the calcination, PVP and other solvents were evaporated except titania and copper. EDX spectra confirm that after calcination we have pure copper doped titania NFs.

The post calcined samples were rougher and have porous structures due to the evaporation of PVP and organic contents. Mesoporous structures were found in the annealed NFs. These structures not only provide suitable energy levels for efficient charge transportation from dye molecules but also continuous structures for better charge mobility [8]. Continuous structure of NFs was observed for calcined samples. These continuous structures are very helpful in charge transport and provide high charge mobility due to less discontinuity of the path [9]. Thus, these structures can improve the current density and power conversion efficiency of the solar cell.

Table 3. Atomic %age of different elements in bare TiO_2 NFs and Cu-Doped TiO_2 NFs

Sample	***Ti***	***O***	***Cu***	***C***	***Cl***
TiO_2 Nanofibers	*3.74*	*75.16*	*0.06*	*20.70*	*0.03*
Cu-TiO_2 Nanofibers	*20.62*	*79.22*	*0.17*	*0*	*0*
NOTE: *Ti-Titanium, O-Oxygen, Cu-Copper, C-Carbon, Cl-Chlorine.*					

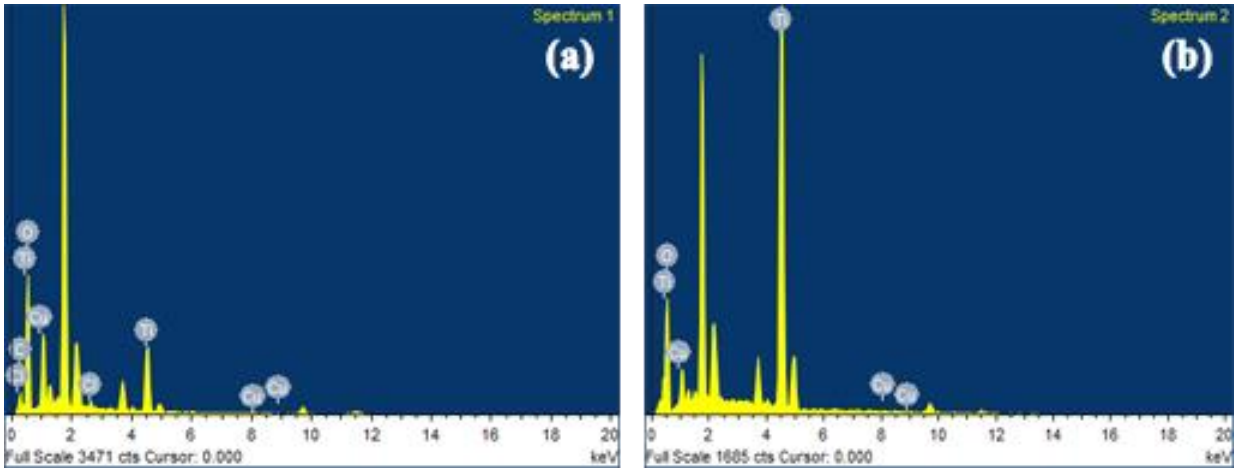

Figure 1: a) EDX spectra for uncalcined sample b) EDX data for calcined at 500°C

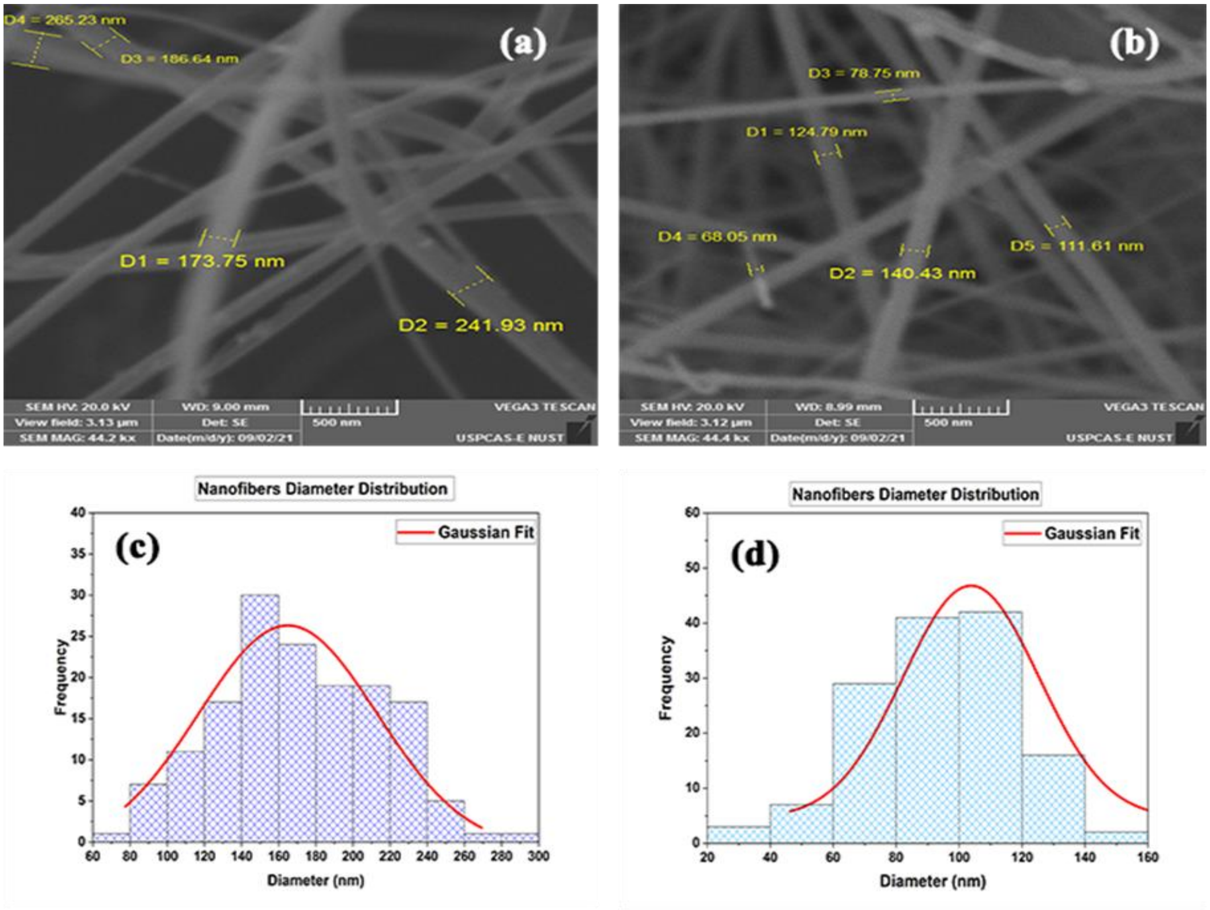

Figure 2: a) 3% Cu doped TiO_2 before calcination b) 3% Cu doped TiO_2 after calcination c) Histogram and Gaussian fitting on uncalcined sample d) Histogram and Gaussian fitting on calcined sample at 500°C.

4.2 Structural Analysis

FTIR was used to analyze the functional group and structural analysis of the desired material. As shown in figure 4. FTIR results reveal that before calcination there was an intense peak of carbon, hydrogenated carbon, and O-H at 1283 cm^{-1}, 1426 cm^{-1}, 1539 cm^{-1}, 1630 cm$^{-1,}$ and 3178 cm^{-1}.due to the presence of PVP, solvents, water, and a hydroxyl group. The presence of anatase copper doped titania was in the range of 400 cm^{-1} to 800 cm^{-1}. These results are much correlated to the previous findings [10]. After calcination at 500°C, there was no peak of carbon and C-H except anatase titania on the FTIR spectra because the evaporation point of PVP is below 400 to 450°C. The peak after calcination validates that there was no presence of water, hydroxyl, and hydrocarbon in NFs after the heating treatment. Only nanofibers of Cu-doped Titania were left behind after the calcination of the material.

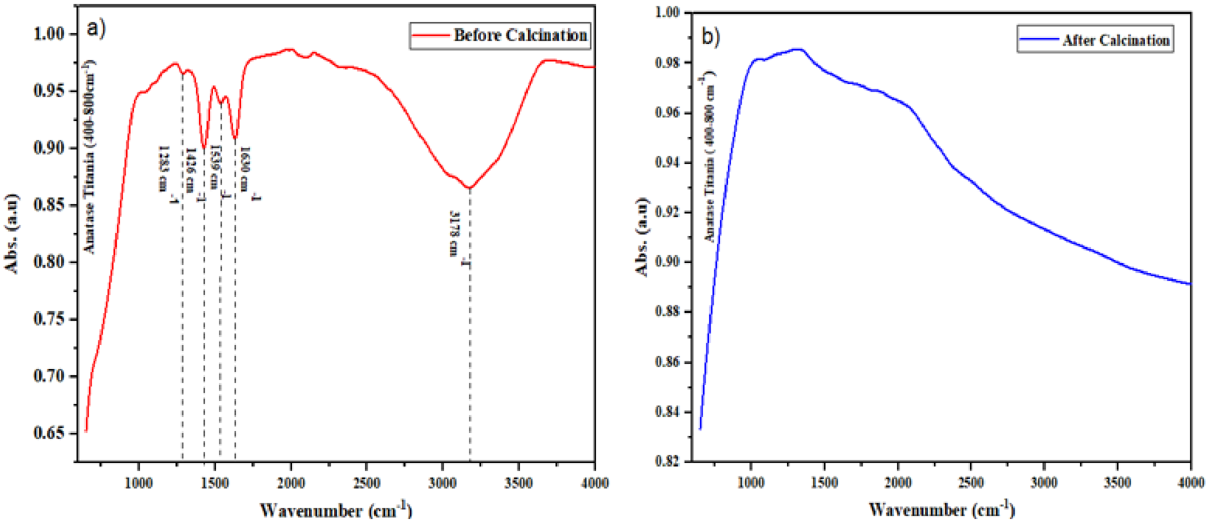

Figure 3: a) FTIR spectra before calcination b) FTIR spectra after calcination at 500°C

4.3 Optical Properties

To analyze the optical properties of photoanode UV-Vis was performed and is displayed in figure 4. Bare TiO_2 NFs have a bandgap of 3.7 eV and the maximum absorption of the spectrum was around 314 nm. The absorption peaks are obtained when an electron is excited to the conduction band (CB) from the Valence band (VB). However, there was negligible absorbance beyond 314nm which shows that the absorption in the visible region of the EM spectrum is nearly equal to zero. At 3% Cu doped TiO_2 NFs has a bandgap of 4.25 eV and absorption of the spectrum was from 250 nm to 285 nm. Negligible absorbance was observed beyond 285nm. Most of the spectrum was absorbed in the ultraviolet (UV) region of the irradiation. The UV-vis of Cu-TiO2 NFs shows the shift of absorbance towards the UV region. Due to the substitution of Cu^{2+} in the lattice structure of TiO_2, defects are generated which causes a change in optical response. When Titania is doped with metals the material properties to Titania are altered mainly due to the presence of Cu^{2+} ion on the surface as well as inside bulk TiO_2.

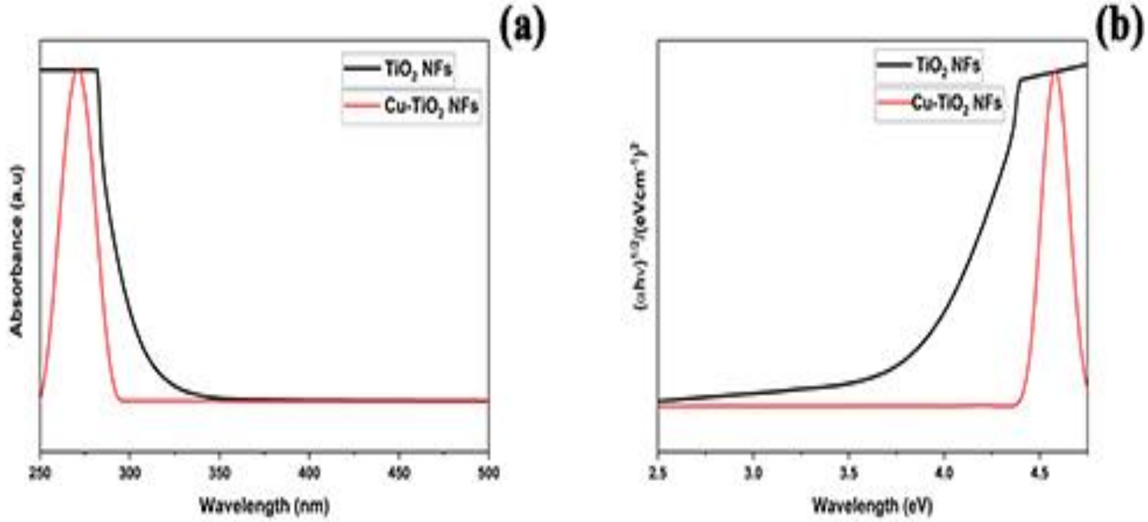

Figure 4: Absorption spectra of Titania and Cu doped Titania Nanofibers.

4.4 Electrical Properties

Electrical properties of the bare TiO_2 NFs and Cu-TiO_2 NFs were analyzed by using the hall effect. Bulk concentration, Conductivity, Resistivity, and semiconductor type were determined by using this technique. For TiO_2 NFs, the carrier concentration was $3.2x10^{11}$, for Cu-TiO2 NFs it was $5.4x10^{12}$ the bulk concentration has increased by 17 times. Due to doping of Cu^{2+} in TiO_2 lattice structure free carriers are generated which increase overall bulk concentration. As the concentration of carriers increased, the conductivity of the copper doped titania also enhanced as shown in table 4 [11]. The conductivity of Cu-TiO_2 NFs was $3.5x10^{-6}$ S/cm, which lie well within the range of semiconductors. It is 2 times more than pure TiO_2 NFs which is attributed due to the large presence of free carriers. The Hall Coefficient of both the samples was negative, therefore they are n-type semiconductors [12].

Table 4. Hall Effect Measurements of simple TiO_2 NFs and Cu-Doped TiO_2 NFs

Sample	***n_H (cm^{-3})***	***ρ (Ω.cm)***	***Σ (1/Ω.cm)***	***Type***
TiO_2 Nanofibers	*$3.2x10^{+11}$*	*$6.5x10^{+05}$*	*$1.5x10^{-06}$*	*n-Type*
Cu-TiO_2 Nanofibers	*$5.4x10^{+12}$*	*$2.9x10^{+05}$*	*$3.5x10^{-06}$*	*n-Type*
NOTE: n_H- Bulk Concentration, ρ-Resistivity, σ-Conductivity.				

5.Conclusion

Bare and Copper doped Titania NFs were successfully synthesized by using the electrospinning technique. SEM results reveal that size of the nanofibers was reduced and rougher after calcination at 500°C. EDS results confirm the presence of copper doping inside the titania. FTIR results elucidate that after calcination only copper doped titania was left behind and there was no peak of carbon, C-H, and a hydroxyl group. UV-Vis results show that bandgap increased after doping at 3% of copper in titania NFs. This is due to the substitution of Cu^{2+} in the lattice structure of TiO_2 the defects are generated which causes a change in optical response. Hall Effect results shown that conductivity of the fibers increased by 2 times after doping of copper in titania NFs. These findings prove that Copper doped Titania has the potential to be utilized as a photoanode semiconductor material in the field of photovoltaics 3rd generation solar cells.

6.Acknowledgment

PGP Directorate research department of the National University of Science and Technology (NUST) Pakistan has financially supported to complete of this Project.

7.References

1. Al-Attafi, K., et al., The effect of amorphous TiO 2 in P25 on dye-sensitized solar cell performance. 2018. 54(4): p. 381-384.

2. Unal, F.A., et al., Synthesis, characterization, and application of transition metals (Ni, Zr, and Fe) doped TiO2 photoelectrodes for dye-sensitized solar cells. 2020. 299: p. 112177.

3. Rajamanickam, N., K.J.J.o.C. Ramachandran, and I. Science, Improved photovoltaic performance in nano TiO2 based dye sensitized solar cells: Effect of TiCl4 treatment and Sr doping. 2020. 580: p. 407-418.

4. Nguyen, H.H., et al., Physicochemical properties of Cr-doped TiO2 nanotubes and their application in dye-sensitized solar cells. 2020. 397: p. 112514.

5. Sun, J., et al., Ag-decorated TiO2 nanofibers for highly efficient dye sensitized solar cell. 2020. 260: p. 126882.

6. Sista, D., New Perspective of Nano Fibers: Synthesis and Applications. 2021.

7. Barhoum, A., M. Bechelany, and A.S.H. Makhlouf, Handbook of nanofibers. 2019: Springer.

8. Mali, S.S., et al., Evaluation of various diameters of titanium oxide nanofibers for efficient dye sensitized solar cells synthesized by electrospinning technique: A systematic study and their application. 2015. 166: p. 356-366.

9. Hussein, A.M., et al., Interconnected ZrO2 doped ZnO/TiO2 network photoanode for dye-sensitized solar cells. 2018. 4: p. 56-64.

10. Ansari, Z., et al., Dye sensitized solar cells fabricated using Cu-Doped TiO2 nanopowder with anthocyanin as sensitizer. 2015. 10(2): p. 290-294.

11. Li, R., et al., Influence of charge carriers concentration and mobility on the gas sensing behavior of tin dioxide thin films. 2019. 9(9): p. 591.

12. Mazhir, S.N. and N.H.J.J.o.A.P. Harb, Influence of concentration on the structural, optical and electrical properties of TiO2: CuO thin film Fabricate by PLD. 2015. 7(6): p. 14-21.